ESC-TR-96-125

Quarterly Technical Report

Solid State Research

19971007 157

1997:1

Lincoln Laboratory

MASSACHUSETTS INSTITUTE OF TECHNOLOGY

LEXINGTON, MASSACHUSETTS

Prepared for the Department of the Air Force under Contract F19628-95-C-0002.

Approved for public release; distribution is unlimited.

DTIC QUALITY INSPECTED 4

This report is based on studies performed at Lincoln Laboratory, a center for research operated by Massachusetts Institute of Technology. The work was sponsored by the Department of the Air Force under Contract F19628-95-C-0002.

This report may be reproduced to satisfy needs of U.S. Government agencies.

The ESC Public Affairs Office has reviewed this report, and it is releasable to the National Technical Information Service, where it will be available to the general public, including foreign nationals.

This technical report has been reviewed and is approved for publication.

FOR THE COMMANDER

Gary Tutungian
Administrative Contracting Officer
Contracted Support Management

Non-Lincoln Recipients

PLEASE DO NOT RETURN

Permission is given to destroy this document when it is no longer needed.

MASSACHUSETTS INSTITUTE OF TECHNOLOGY
LINCOLN LABORATORY

SOLID STATE RESEARCH

QUARTERLY TECHNICAL REPORT

1 NOVEMBER 1996 – 31 JANUARY 1997

ISSUED 18 SEPTEMBER 1997

Approved for public release; distribution is unlimited.

LEXINGTON MASSACHUSETTS

ABSTRACT

This report covers in detail the research work of the Solid State Division at Lincoln Laboratory for the period 1 November 1996 through 31 January 1997. The topics covered are Quantum Electronics, Electrooptical Materials and Devices, Submicrometer Technology, High Speed Electronics, Microelectronics, Analog Device Technology, and Advanced Silicon Technology. Funding is provided primarily by the Air Force, with additional support provided by the Army, DARPA, Navy, BMDO, NASA, and NIST.

TABLE OF CONTENTS

	Abstract	iii
	List of Illustrations	vii
	List of Tables	x
	Introduction	xi
	Reports on Solid State Research	xiii
	Organization	xxi
1.	QUANTUM ELECTRONICS	1
1.1	Thermal Coefficients of Refractive Index Optical Path Length for YAG	1
2.	ELECTROOPTICAL MATERIALS AND DEVICES	5
2.1	InGaAsP/InP Materials for $\lambda = 1.5\ \mu$m Lasers and Amplifiers	5
2.2	Use of Proton Bombardment to Reduce the Effects of Photogenerated Free Carriers in Passive-Waveguide Optical Frequency Converters	9
2.3	Microwave Analog Optical Links Using Suboctave Linearized Modulators	14
3.	SUBMICROMETER TECHNOLOGY	21
3.1	Nanochannel Fabrication for Chemical Sensors	21
4.	HIGH SPEED ELECTRONICS	29
4.1	Thickness Inhomogeneity of Electronic Properties of GaN Epilayers	29
5.	MICROELECTRONICS	35
5.1	Adaptive Imaging with an Orthogonal-Transfer CCD	35
6.	ANALOG DEVICE TECHNOLOGY	41
6.1	Superconductive Patch Resonator for Microwave High-Power Filters	41
7.	ADVANCED SILICON TECHNOLOGY	45
7.1	Fully Planar Multilevel Metal Interconnect	45

LIST OF ILLUSTRATIONS

Figure No.		Page
1-1	Diagram of the experimental apparatus.	1
1-2	β and dn/dT at 633 nm for undoped YAG.	2
2-1	Schematic diagram of stepped graded-index (GRIN) separate-confinement-heterostructure (SCH) structure showing the three-quantum-well (3QW) case. The profile on the right-hand edge shows bandgap variation. Values of y represent As fraction of lattice-matched InGaAsP alloys. The optical confinement region of the structure is nominally undoped. The layer thicknesses are those for the normal beam divergence structures.	6
2-2	Net gain, $G-\alpha$, vs current density J for three structures, all with 3QWs. The data on the right are from lattice-matched quantum wells and a two-step SCH structure. The data in the center are from biaxially compressed quantum wells with $\approx 1\%$ strain and a two-step SCH structure. The data on the left are from the strained quantum wells and the stepped GRIN SCH structure.	7
2-3	Net gain, $G-\alpha$, vs current density J for stepped GRIN SCH with SQW, 3QWs, and 5QWs. In all cases the quantum wells are biaxially compressed with $\approx 1\%$ strain.	7
2-4	Response of SQW ridge waveguides: (a) experimental (squares) and calculated (dashed lines) relative pump transmission vs pump power, and (b) experimental (plus signs) and calculated (dashed lines) four-wave mixing conversion efficiency vs pump power. In (a) and (b), the $\tau = 0$ ns curves represent the results expected from two-photon absorption alone.	10
2-5	Low-temperature photoluminescence spectra of unbombarded and bombarded SQW wavelength-converter samples.	12
2-6	Results of Fabry-Perot loss measurements on unbombarded and proton-bombarded SQW and 3QW wavelength-conversion samples.	13
2-7	Projected CW conversion efficiency vs pump power of SQW and 5QW devices assuming elimination of excess loss due to accumulation of photogenerated free carriers. The parameters used in the calculation are based on $\chi^{(3)}$ and loss values obtained from low-power measurements on our initial SQW devices.	13
2-8	Configuration of experimental links which employ two Mach-Zehnder modulators in series.	15

LIST OF ILLUSTRATIONS (Continued)

Figure No.		Page
2-9	Third-order intermodulation suppression vs frequency: (a) 900-MHz link, modulation depth *m(V)* = 0.13 per frequency at 900 MHz, and (b) 2-GHz link, *m(V)* = 0.27 per frequency at 2.1 GHz. The modulator bias points were set for minimum two-tone intermodulation at the frequencies indicated by the arrows; then the two frequencies (1-MHz separation) were swept over the band to produce the plot.	17
3-1	Schematic diagram of a chemical charge-coupled device (CCD): (a) distribution of ions in channel for all electrodes being positively charged with respect to the electrolyte reservoir, (b) ion distribution when first electrode at reservoir is negatively charged, and (c) ion distribution after positive ion packet is stepped four electrodes to right. A new positive ion packet is being formed under the first electrode.	22
3-2	Simulated ion current per step of Li^+ and H^+ ions through chemical CCD as function of stepping frequency. The CCD electrodes were assumed to be on 1-μm centers for the theoretical results shown here.	23
3-3	Predicted ability of chemical CCD to concentrate ions. The calculations assumed 1-μm-long CCD electrodes and three stepping frequencies of 100, 1000, and 1100 Hz. The concentration ratio is plotted as a function of diffusion coefficient. The diffusion constants of several ions in water are shown for comparison.	24
3-4	Overview of channel structure layout and schematic cross section of Si nanochannel.	25
3-5	Scanning electron micrograph of channel fabricated in Si. This channel is 1 μm wide, 50 nm high, and > 1 mm in length.	26
3-6	Graph of 5-μm-wide channels, 100 nm high, etched for up to 80 h.	26
4-1	(a) Electron concentration vs reciprocal temperature and (b) electron mobility vs temperature for *n*-type GaN films grown by hydride vapor phase epitaxy (HVPE). Films are of three different thicknesses as determined from variable-temperature Hall-effect measurements.	30
4-2	Net donor concentration (N_D^+-N_A) for HVPE-grown *n*-type GaN as determined by capacitance-voltage measurements on Au Schottky diodes for three different film thicknesses. The inset demonstrates the net donor depth profile for a film thickness of 7 μm.	31
4-3	Deep-level transient spectroscopy spectrum for HVPE-grown *n*-type GaN (original film thickness). The peaks in the spectrum indicate the presence of discrete deep levels. The parameters (concentration *N*, and activation energy for electron emission to the conduction band, ΔE) for three deep levels are depicted for three different film thicknesses *d*.	32

LIST OF ILLUSTRATIONS (Continued)

Figure No.		Page
5-1	Basic cell layout of the orthogonal-transfer charge-coupled device (OTCCD), and modes of clocking for (a) vertical and (b) horizontal charge transfer.	35
5-2	Photograph showing four pixels in imaging array of OTCCD. The pixel size is 15×15 μm.	36
5-3	Operation of OTCCD as adaptive sensor for tip/tilt correction of astronomical images. The frame store is used as a fast star tracker to follow the image motion, and this information is used in turn to clock the imaging array gates.	37
5-4	Portion of image of M71 using (a) standard clocking and (b) the adaptive clocking method illustrated in Figure 5-3. The image resolution on the top has a full width at half-maximum of 0.73 arc sec, while on the bottom this has been improved to 0.50 arc sec.	38
6-1	Lime resonator made using sputtered YBCO films deposited on both sides of $LaAlO_3$ substrate.	43
6-2	Circulating power (left axis) and unloaded Q (right axis) as a function of input power for resonator shown in Figure 6-1.	44
7-1	Scanning electron micrograph cross section of dielectric gap fill: (a) standard deposition, aspect ratio ~ 0.95; (b) multiple deposition/etch back process, aspect ratio ~ 1.35.	46
7-2	Chemical-mechanical planarization (CMP) step height reduction. Measurements shown are (a) before and (b) after CMP.	47
7-3	Comparison of (a) nonplanar and (b) planar interconnect in silicon-on-insulator ring oscillator.	48

LIST OF TABLES

Table No.		Page
2-1	Summary of Broad-Area Laser Properties for Various Structures	8
2-2	Optical Link Performance	16
6-1	Relative Circulating Power for Various Resonators	43

INTRODUCTION

1. QUANTUM ELECTRONICS

The change in refractive index at 633 nm with temperature and the change in optical path length with temperature in YAG have been measured in the temperature range 85 to 285 K. These quantities are substantially smaller at low temperature than at room temperature.

2. ELECTROOPTICAL MATERIALS AND DEVICES

In an investigation of InGaAsP/InP quantum-well (QW) structures for use as diode lasers and optical amplifiers at 1.5-μm wavelength, a graded-index optical confinement structure has been shown to work well for devices, and it avoids the need for growth interruptions. The number of QWs, the width of the confinement region, and the QW strain have been varied to achieve improved gain-saturation and beam-divergence characteristics as well as polarization-insensitive operation.

Experimental results on proton-bombarded QW ridge waveguides indicate that an appropriate low-dose bombardment should minimize photogenerated free-carrier losses in passive 1.5-μm optical frequency converters based on four-wave mixing. Calculations based on the results predict that conversion efficiencies of ≥ -10 dB should be obtainable for pump powers < 100 mW.

Linearized analog fiber-optic links have been developed at frequencies up to 4 GHz. The configuration that provides enhanced linearity uses two integrated optical Mach-Zehnder interferometric modulators in series to reduce third-order intermodulation distortion.

3. SUBMICROMETER TECHNOLOGY

A new chemical sensor has been designed based on the electrostatic interactions between ions in a capillary channel and a series of biased-gate electrodes. The operation of this device has been simulated and a process has been developed to fabricate the capillary channels.

4. HIGH SPEED ELECTRONICS

The electronic properties of heteroepitaxial GaN have been investigated for unintentionally doped, *n*-type films grown by hydride vapor phase epitaxy on sapphire substrates. The room-temperature electron concentrations as determined by Hall-effect measurements were found to increase from ~ 10^{17} cm^{-3} (13 μm) to ~ 10^{20} cm^{-3} (1.2 μm) with decreasing film thickness, but capacitance-voltage and deep-level transient spectroscopy measurements revealed that the ionized, effective donor and deep-level concentrations, respectively, remained unchanged in regions close to the top surface of the films—findings that are consistent with the presence of a thin, highly conductive near-interface layer that acts as a parasitic, parallel conduction path.

5. MICROELECTRONICS

A 512 × 512-pixel charge-coupled device imager capable of charge transfer in all four directions has been fabricated and tested as an image-motion-adaptive sensor at an observatory. The device is able to perform the tip/tilt correction for atmospheric phase distortions, and measurements at Kitt Peak have demonstrated that it can remove ~ 0.5 arc sec of image broadening in quadrature with the remaining sources of distortion.

6. ANALOG DEVICE TECHNOLOGY

A novel superconductive YBaCuO patch resonator has been demonstrated with measured power-handling capability more than 10 times higher than wide-line microstrip resonators. The resonators are designed to be readily concatenated into planar multipole filters.

7. ADVANCED SILICON TECHNOLOGY

A fully planar multilevel metallization process for advanced CMOS projects has been developed, whose features include a gap fill technique for dielectric layers, chemical-mechanical planarization (CMP) of interlevel dielectrics, and damascene aluminum contact and via plug formation by CMP. The process has been used successfully on the first silicon-on-insulator multi-project run.

REPORTS ON SOLID STATE RESEARCH

1 NOVEMBER 1996 THROUGH 31 JANUARY 1997

PUBLICATIONS

Title	Authors	Citation
Use of Charge-Coupled Device Imagers for Charged-Particle Spectroscopy	B. E. Burke R. D. Petrasso* C. K. Li* T. C. Hotaling	*Rev. Sci. Instrum.* **68**, 599 (1997)
Antimonide-Based Strained Quantum-Well Diode Lasers	H. K. Choi G. W. Turner	*Physica Scripta* **T69**, 17 (1997)
Calorimetric Measurements of Optical Materials for 193 nm Lithography	A. Grenville* R. Uttaro J. H. C. Sedlacek M. Rothschild D. Corliss*	*J. Vac. Sci. Technol. B* **14**, 4184 (1996)
Design of an Electronic Charged Particle Spectrometer to Measure <*ρR*> on Inertial Fusion Experiments	D. G. Hicks* C. K. Li* R. D. Petrasso* F. H. Séguin* B. E. Burke J. P. Knauer* S. Cremer* R. L. Kremens* M. D. Cable* T. W. Phillips*	*Rev. Sci. Instrum.* **68**, 589 (1997)
Plasma-Deposited Silylation Resist for 193 nm Lithography	M. W. Horn B. E. Maxwell R. B. Goodman R. R. Kunz L. M. Eriksen	*J. Vac. Sci. Technol. B* **14**, 4207 (1996)

*Author not at Lincoln Laboratory.

CH_3I Vapor Etching of GaAs in a Vertical Rotating-Disk Reactor	C. W. Krueger S. Patnaik* C. A. Wang M. Flytzani-Stephanopoulos*	*J. Cryst. Growth* **169**, 51 (1996)
Turn-Key, Liquid-Nitrogen-Cooled 3.9-μm Semiconductor Laser Package with 0.2W CW Output	H. Q. Le G. W. Turner J. R. Ochoa	*Electron. Lett.* **32**, 2359 (1996)
Broad Wavelength Tunability of Grating-Coupled External Cavity Midinfrared Semiconductor Lasers	H. Q. Le G. W. Turner J. R. Ochoa M. J. Manfra C. C. Cook Y.-H. Zhang*	*Appl. Phys. Lett.* **69**, 2804 (1996)
Surface Vapor Transport for Accurate Microoptics in Compound Semiconductors	Z. L. Liau	*Mater. Chem. Phys.* **46**, 265 (1996)
Growth of Fluorocarbon Polymer Thin Films with High CF_2 Fractions and Low Dangling Bond Concentrations by Thermal Chemical Vapor Deposition	S. J. Limb* C. B. Labelle* K. K. Gleason* D. J. Edell* E. F. Gleason	*Appl. Phys. Lett.* **68**, 2810 (1996)
Terahertz Measurements of Resonant Planar Antennas Coupled to Low-Temperature-Grown GaAs Photomixers	K. A. McIntosh E. R. Brown K. B. Nichols O. B. McMahon W. F. DiNatale T. M. Lyszczarz	*Appl. Phys. Lett.* **69**, 3632 (1996)
Investigation of Ultrashort Photocarrier Relaxation Times in Low-Temperature-Grown GaAs	K. A. McIntosh K. B. Nichols S. Verghese E. R. Brown	*Appl. Phys. Lett.* **70**, 354 (1996)

*Author not at Lincoln Laboratory.

Gallium Nitride Thick Films Grown by Hydride Vapor Phase Epitaxy	R. J. Molnar P. Maki R. Aggarwal Z. L. Liau E. R. Brown I. Melngailis W. Götz L. T. Romano N. M. Johnson	*Mater. Res. Soc. Symp. Proc.* **423**, 221 (1996)
A 9-Bit Charge-to-Digital Converter for Integrated Image Sensors	S. A. Paul H.-S. Lee*	*Electron. Design* **31**, 1931 (1996)
Sub-Poisson Statistics Observed in an Electronically Shuttered and Back-Illuminated CCD Pixel	R. K. Reich	*IEEE Trans. Electron Devices* **44**, 69 (1997)
High-Performance Charge-Coupled-Device Imager Technology for Plasma Diagnostics	R. K. Reich W. M. McGonagle J. A. Gregory R. W. Mountain B. B. Kosicki E. D. Savoye	*Rev. Sci. Instrum.* **68**, 922 (1997)
How Practical Is 193 nm Lithography?	M. Rothschild J. A. Burns S. G. Cann A. R. Forte C. L. Keast R. R. Kunz S. C. Palmateer J. H. C. Sedlacek R. Uttaro A. Grenville* D. Corliss*	*J. Vac. Sci. Technol. B* **14**, 4157 (1996)
In Situ Concentration Monitoring in a Vertical OMVPE Reactor by Fiber-Optics-Based Fourier Transform Infrared Spectroscopy	S. Salim* C. A. Wang R. D. Driver* K. F. Jensen*	*J. Cryst. Growth* **169**, 443 (1996)

*Author not at Lincoln Laboratory.

Methyl- and Ethyl-Based Organometallic Sources for GaSb Growth	C. A. Wang	*Metalorganic News* **10**, 2 (1996)
Electronic Imaging Aids for Night Driving: Low-Light CCD, Uncooled Thermal IR, and Color Fused Visible/ LWIR	A. M. Waxman E. D. Savoye D. A. Fay M. Aguilar A. N. Gove J. E. Carrick J. P. Racamato	*Proc. SPIE* **2902**, 62 (1996)

ACCEPTED FOR PUBLICATION

Self-Aligned Pseudomorphic HEMT with a Low-Temperature-Grown GaAs Gate	C. L. Chen L. J. Mahoney S. D. Calawa K. M. Molvar	*Electron. Lett.*
Properties of Ferrites at Low Temperatures	G. F. Dionne	*J. Appl. Phys.*
Three-Dimensional Metallodielectric Photonic Crystals Exhibiting Infrared Stop Bands	K. A. McIntosh L. J. Mahoney K. M. Molvar O. B. McMahon	*Appl. Phys. Lett.*
The Growth of Gallium Nitride Vapor Phase Epitaxy	R. Molnar	*J. Cryst. Growth*
Pressure Induced Deep Gap State of Oxygen in GaN	R. Molnar	*Phys. Rev. Lett.*
Linear and Nonlinear Microwave Dynamics of Vortices in $YBa_2Cu_3O_{7-\delta}$ Thin Films	D. E. Oates D. A. Feld N. Belk* G. Dresselhaus* M. Dresselhaus*	*Phys. Rev. B*

*Author not at Lincoln Laboratory.

GaInAsSb/AlGaAsSb Multiple-Quantum-Well Diode Lasers Grown by Organometallic Vapor Phase Epitaxy	C. A. Wang H. K. Choi	*Appl. Phys. Lett.*
PPLN Optical Parametric Amplifiers Pumped by High-Power Passively *Q*-Switched Microchip Lasers	J. J. Zayhowski	*Opt. Lett.*

PRESENTATIONS†

193-nm Lithography	M. Rothschild	Optic and Quantum Electronic Seminar Series, Massachusetts Institute of Technology, Cambridge, Massachusetts, 6 November 1996
193-nm Lithography	M. Rothschild A. R. Forte M. W. Horn R. R. Kunz S. C. Palmateer J. H. C. Sedlacek	IEEE Lasers and Electro-Optics Society Annual Meeting, Boston, Massachusetts, 18-21 November 1996
Diode-Laser-Pumped Solid-State Lasers	T. Y. Fan	Lincoln Laboratory Technical Seminar Series, University of Pittsburgh, Pittsburgh, Pennsylvania, 25 November 1996
Superconductive Passive Microwave Devices	W. G. Lyons	Lincoln Laboratory Technical Seminar Series, Georgia Institute of Technology, Atlanta, Georgia, 26 November 1996

†Titles of presentations are listed for information only. No copies are available for distribution.

Title	Authors	Venue
Optical Lithography at Feature Sizes of 0.25 μm and Below	M. W. Horn	Lincoln Laboratory Technical Seminar Series, Pennsylvania State University, University Park, Pennsylvania, 2 December 1996; Colorado State University, Fort Collins, Colorado, 3 December 1996; Massachusetts Institute of Technology, Cambridge, Massachusetts, 15 January 1997
Resonant-Tunneling Diode Digital Filters	T. C. L. G. Sollner	Advanced Heterostructure Workshop '96, Kona Coast, Hawaii, 2-6 December 1996
Vortex Dynamics in YBCO Thin-Film Josephson Edge Junctions: Mechanisms for Non-Linear Microwave and dc Power Dependence	Y. M. Habib* D. E. Oates G. Dresselhaus* M. Dresselhaus*	1996 Fall Meeting of the Materials Research Society, Boston, Massachusetts, 2-6 December 1996
Thickness Dependence of Electronic Properties of GaN Epilayers	R. Molnar	
Measurements and Modeling of Microwave Power Dependence in YBCO Thin-Film Josephson Edge Junctions: Direct Observation of Josephson Fluxons	D. E. Oates Y. M. Habib* C. J. Lehner* N. Belk* G. Dresselhaus* M. S. Dresselhaus*	
InAsSb/InAlAsSb Quantum-Well Diode Lasers Emitting between 3 and 4 μm	G. W. Turner H. K. Choi M. J. Manfra M. K. Connors	

*Author not at Lincoln Laboratory.

GaInAsSb Materials for Thermophotovoltaics	C. A. Wang G. W. Turner H. K. Choi D. L. Spears	1996 Fall Meeting of the Materials Research Society, Boston, Massachusetts, 2-6 December 1996
Novel Semiconductor Lasers, Microoptics and Integrated Optoelectronics: Microfabrication by Surface-Energy Processes	Z. L. Liau	Lincoln Laboratory Technical Seminar Series, University of California/ San Diego, La Jolla, California, 6 December 1996
Tip Field Suppression due to Space Charge and Its Implications for Field Emitter Array Characterization	R. A. Murphy K. L. Jensen M. A. Kodis* E. G. Zaidman*	International Electron Devices Meeting, San Francisco, California, 8-11 December 1996
Solid-State Laser Development at Lincoln Laboratory	T. Y. Fan	IEEE Technical Seminar, National Research Council, Ottawa, Ontario, Canada, 11 December 1996
Advanced Detection Methods in Cone Penetrometer Screening for Explosives	J. J. Zayhowski B. Johnson N. Newbury J. Worhoudt* J. H. Shorter* C. E. Kolb*	Environmental Quality Research Program Grantee/ Contractor Meeting, Panama City, Florida, 13-17 January 1997
RF Phase Noise in Externally Modulated Analog Optical Links	G. E. Betts C. D. Cherry C. H. Cox III F. J. O'Donnell	7th Annual DARPA Symposium on Photonics Systems for Antenna Applications, Monterey, California, 14 January 1997
Photolithography with Sources below 200 nm	M. Rothschild J. H. C. Sedlacek D. Corliss	12th Topical Meeting, Optical Society of America, Orlando, Florida, 27-29 January 1997

*Author not at Lincoln Laboratory.

ORGANIZATION

SOLID STATE DIVISION

D. C. Shaver, *Head*
R. W. Ralston, *Associate Head*
N. L. DeMeo, Jr., *Assistant*

D. Abusch-Magder, *Research Assistant*
J. W. Caunt, *Assistant Staff*
K. J. Challberg, *Administrative Staff*
J. D. Pendergast, *Administrative Staff*

SUBMICROMETER TECHNOLOGY

M. Rothschild, *Leader*
T. M. Lyszczarz, *Assistant Leader*
L. H. Dubois, *Senior Staff*†

Astolfi, D. K.
Bloomstein, T. M.
Craig, D. M.
DiNatale, W. F.
Doran, S. P.
Efremow, N. N., Jr.
Forte, A. R.
Geis, M. W.
Goodman, R. B.
Horn, M. W.
Krohn, K. E.
Kunz, R. R.
Liberman, V.
Maki, P. A.
Palmacci, S. T.
Palmateer, S. C.
Reinold, J. H., Jr.
Sedlacek, J. H. C.
Stern, M. B.
Twichell, J. C.
Uttaro, R. S.

QUANTUM ELECTRONICS

A. Sanchez-Rubio, *Leader*
T. Y. Fan, *Assistant Leader*

Aggarwal, R. L.
Cook, C. C.
Daneu, J. L.
Daneu, V.
DiCecca, S.
Dill, C., III
Jeys, T. H.
Le, H. Q.
Ochoa, J. R.
Zayhowski, J. J.

ELECTROOPTICAL MATERIALS AND DEVICES

B. Y. Tsaur, *Leader*
D. L. Spears, *Assistant Leader*
R. C. Williamson, *Senior Staff*

Bailey, R. J.
Betts, G. E.
Chen, C. K.
Choi, H. K.
Choi, S. S.*
Connors, M. K.
Cronin, S.*
Donnelly, J. P.
Goodhue, W. D.
Harman, T. C.
Herrmann, F. P.
Liau, Z. L.
Manfra, M. J.
Missaggia, L. J.
Mull, D. E.
Napoleone, A.
Nee, P.*
Nitishin, P. M.
Oakley, D. C.
O'Donnell, F. J.
Paul, S. A.*
Poillucci, R. J.
Reeder, R. E.
Royter, Y.*
Santiago, D. D.
Turner, G. W.
Walpole, J. N.
Wang, C. A.

---

* Research Assistant
† Intergovernmental Personnel Act assignment

HIGH SPEED ELECTRONICS

M. A. Hollis, *Leader*
E. R. Brown, *Assistant Leader*†

Bozler, C. O.
Calawa, A. R.‡
Calawa, S. D.
Chen, C. L.
Graves, C. A.
Harris, C. T.
Mahoney, L. J.
Mathews, R. H.
McIntosh, K. A.
McMahon, O. B.
Molnar, R. J.
Rabe, S.
Rathman, D. D.
Verghese, S.
Young, A. M.

ANALOG DEVICE TECHNOLOGY

T. C. L. G. Sollner, *Leader*
L. M. Johnson, *Assistant Leader*
A. C. Anderson, *Senior Staff*

Ala'ilima, T. F.
Arsenault, D. R.
Berggren, V.
Boisvert, R. R.
Feld, D. A.
Fitch, G. L.
Hamm, J. M.
Holtham, J. H.
Lyons, W. G.
Macedo, E. M., Jr.
McClure, D. W.
Murphy, P. G.
Oates, D. E.
Sage, J. P.
Seaver, M. M.
Slattery, R. L.

MICROELECTRONICS

E. D. Savoye, *Leader*
B. B. Kosicki, *Associate Leader*
B. B. Burke, *Senior Staff*

Aull, B. F.
Daniels, P. J.
Doherty, C. L., Jr.
Dolat, V. S.
Donahue, T. C.
Felton, B. J.
Gregory, J. A.
Hotaling, T. C.
Johnson, K. F.
Lind, T. A.
Loomis, A. H.
McGonagle, W. H.
Percival, K. A.
Reich, R. K.
Young, D. J.

ADVANCED SILICON TECHNOLOGY

C. L. Keast, *Leader*
P. W. Wyatt, *Associate Leader*

Berger, R.
Burns, J. A.
Davis, P. V.
D'Onofrio, R. P.
Frankel, R. S.
Fritze, M.
Knecht, J. M.
Liu, H. I.
Newcomb, K. L.
Sexton, S. V.
Soares, A. M.
Suntharalingam, V.
Wachtmann, B. K.
Young, G. R.

‡Part Time
†Intergovernmental Personnel Act assignment

1. QUANTUM ELECTRONICS

1.1 THERMAL COEFFICIENTS OF REFRACTIVE INDEX OPTICAL PATH LENGTH FOR YAG

The average power in solid state lasers is limited primarily by thermo-optic effects in the solid state gain medium. These effects include stress fracture, stress-induced birefringence, and thermo-optic distortion of the gain element. Desired properties of the solid state gain medium for high-power lasers include high thermal conductivity, large rupture stress, low thermal expansion, small change in refractive index with temperature, and low heat deposited in the gain medium. The change in optical path length with temperature and the change in refractive index with temperature in YAG is measured from 85 to 285 K in order to help estimate the improvement that might be expected in a cooled laser.

The optical path length is given by nL, where n is the refractive index of the material and L is its physical length. The change in optical path length with temperature is measured by observing interference fringes (Fizeau fringes) between two surfaces of the optical medium as the medium is ramped in temperature, as shown in Figure 1-1 [1]. One fringe cycle corresponds to a round-trip optical path length change of one optical wavelength. From the period of the interference fringe pattern, the fractional change in optical path length with temperature, β, can be determined where

$$\beta = \frac{1}{nL}\frac{d(nL)}{dT} \ . \tag{1.1}$$

In our experiment, a He-Ne laser operating at 633 nm was the light source and the optical medium is a 15.01-mm-long piece of undoped YAG. The measurement of β was at five discrete temperatures. The temperature was ramped around each of these temperatures by ± 5 K for the three highest temperature data points and by ± 10 K for the two lowest temperature data points; the larger ramp for the lower data points was needed because of the substantially lower β at these temperatures. A sinusoid is fitted to the output of the photodiode as a function of temperature, and the period of the sinusoid is used to calculate β.

The change in refractive index with temperature dn/dT can be calculated from β and the thermal expansion coefficient α using

$$\beta = \alpha + \frac{1}{n}\frac{dn}{dT} \ . \tag{1.2}$$

where

$$\alpha \frac{1}{L}\frac{dL}{dT} \ . \tag{1.3}$$

An approximation for α for YAG in the temperature range 100–296 K can be obtained by [2]

$$\alpha = 1.78 \times 10^{-6} + 3.3 \times 10^{-8} T \ , \tag{1.4}$$

where T is in degrees Kelvin. In the calculation for dn/dT we assume that this expression is valid at 85 K. In YAG at 633 nm, n = 1.823. The results are shown in Figure 1-2. The data near room temperature are

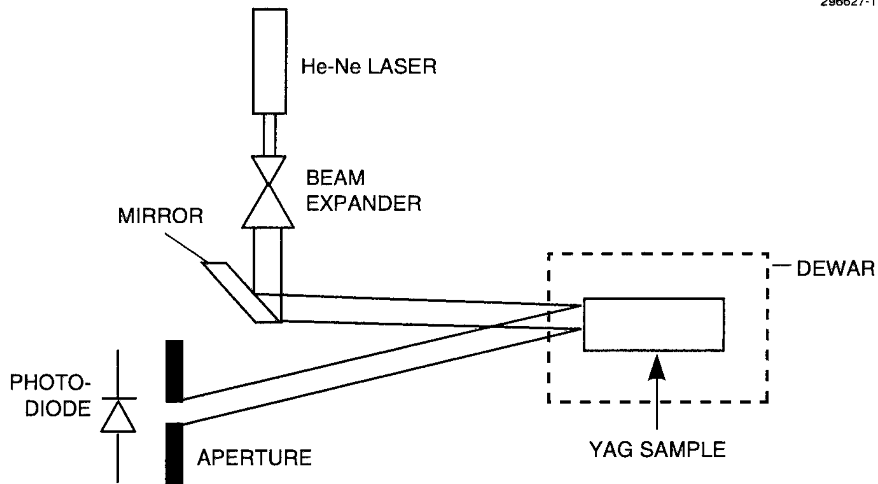

Figure 1-1. Diagram of the experimental apparatus.

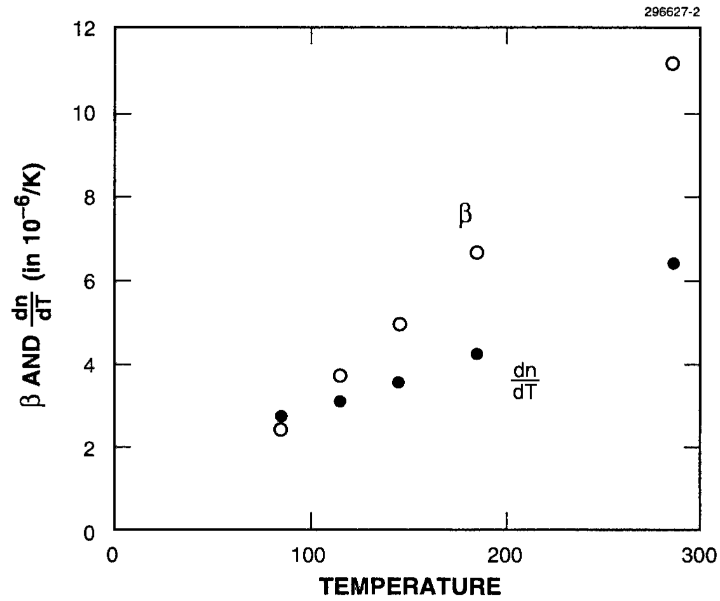

Figure 1-2. β and dn/dT at 633 nm for undoped YAG.

in reasonable agreement with previously published data [1]. At 100 K, *dn/dT* is approximately 40% of the value at room temperature, which means that thermal lensing and thermo-optic distortions in YAG laser gain media will be substantially less at low temperatures than at room temperature.

T. Y. Fan
J. L. Daneu

REFERENCES

1. J. D. Foster and L. M. Osterink, *Appl. Opt.* **7**, 2428 (1968).
2. D. Taylor, *Br. Ceram. Trans. J.* **86**, 1 (1987).

2. ELECTROOPTICAL MATERIALS AND DEVICES

2.1 InGaAsP/InP MATERIALS FOR $\lambda = 1.5$ μm LASERS AND AMPLIFIERS

Previously we reported on characterization of InGaAsP/InP quantum-well structures grown by organometallic vapor phase epitaxy (OMVPE) for diode lasers and optical amplifiers at 1.3-μm wavelength [1],[2]. Those results equaled or bettered values reported in the literature. The present work uses appropriately shifted alloys for operation at 1.5-μm wavelength. Additionally, continuously graded alloys, used in a graded-index (GRIN) separate-confinement heterostructure (SCH), eliminate growth interruptions that could otherwise only be avoided by adding OMVPE sources. The graded region is inserted between a large-bandgap alloy and the barrier, as shown in Figure 2-1, in a configuration termed a stepped GRIN SCH.

As in the previous work, growth has been carried out at atmospheric pressure in a chimney-geometry reactor that incorporates susceptor rotation [3]. For the most part, the procedures have closely followed those reported in Refs. 1 and 2. The continuously graded layers, unusual for InGaAsP/InP, have been grown with fixed flows of trimethylindium and phosphine and ramped flows of trimethylgallium and arsine. The ramped components have been provided from double-dilution sources, which have advantages over direct sources for time-varying flows.

An observation we have not seen previously reported concerns the integrity of the quantum-well structure. Initially, both quantum-well and barrier layers were grown at rates in the range 0.2–0.3 nm/s. Some structures exhibited a slight surface roughness under differential interference contrast and atomic force microscopy, and showed no evidence of quantum-well structure in photoluminescence or x-ray diffraction. The same problem could occur for 1.3-μm-wavelength structures, as well as for lattice-matched and for biaxially strained quantum wells. After considerable experimentation, we have determined that the problem can be reproducibly eliminated by increasing the quantum-well and barrier growth rates to > 0.3 nm/s.

Grown wafers have been fabricated into broad-area lasers and characterized by measurements of threshold current density and differential quantum efficiency vs cavity length. Also, beam widths perpendicular to the plane of the junction have been measured in the far field.

Several steps, using three quantum wells (3QWs), have been taken to arrive at the structure shown in Figure 2-1. The improvements, as measured by net gain vs current density, are shown in Figure 2-2. First, the quantum-well alloys have been changed from lattice-matched to biaxially compressed with about 1% strain. Then, the stepped SCH has been replaced with the stepped GRIN SCH. The threshold current densities for 3-mm-long cavities, J_t[3 mm], have decreased from the 300- to 400-A/cm^2 range, to the 200- to 250-A/cm^2 range, to the 180- to 200-A/cm^2 range with these respective changes.

The lowest value for the 1.3-μm 3QW lasers was J_t[3 mm] = 176 A/cm^2, for comparison. Measurements have yet to be made on 1.3-μm devices in the stepped GRIN SCH configuration.

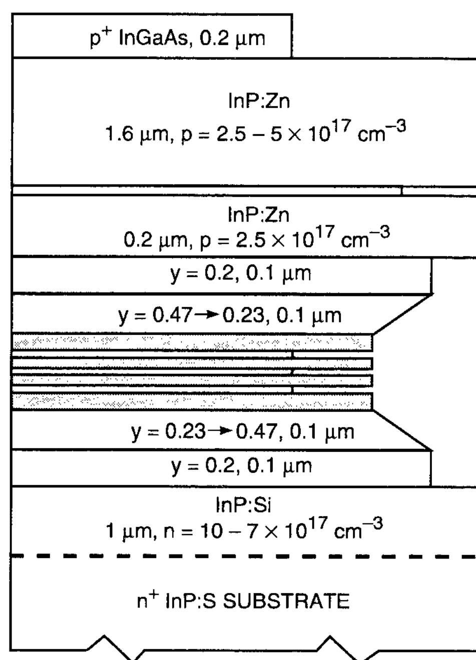

Figure 2-1. Schematic diagram of stepped graded-index (GRIN) separate-confinement-heterostructure (SCH) structure showing the three-quantum-well (3QW) case. The profile on the right-hand edge shows bandgap variation. Values of y represent As fraction of lattice-matched InGaAsP alloys. The optical confinement region of the structure is nominally undoped. The layer thicknesses are those for the normal beam divergence structures.

With the 1.5-μm-wavelength stepped GRIN SCH structures, a comparison has been made of behavior with one, three, and five biaxially compressed quantum wells. With the increases in quantum-well number, J_t[3 mm] increased from 150 A/cm^2 for the single quantum well (SQW) to the 180- to 200-A/cm^2 range for 3QWs, and then to the 285- to 290-A/cm^2 range for 5QWs. Figure 2-3 shows the net gain vs J behavior for different numbers of quantum wells.

The beam divergence for these devices varied from 37° full width at half-maximum (FWHM) for the SQW to 40° FWHM for 5QWs. Structures with 3QWs and 5QWs also have been grown with reduced thicknesses of optical confinement layers. This increases the guided beam width and reduces the divergence angle. For 3QW devices, the divergence has been reduced from 39° to 33° FWHM, and for 5QW devices it has been reduced from 40° to 32°. The thicknesses given in Figure 2-1 are typical of the 3QW structure with 39° FWHM. To obtain the 33° FWHM, the thickness of the y = 0.2 alloy was reduced to 0.02 μm, and that of the tapered region was reduced to 0.05 μm. The smaller confinement factor and increased loss due to optical tailing in the cladding region caused J_t[3 mm] to increase from 180 to 270 A/cm^2 for 3QWs and to increase from 285 to 390 A/cm^2 for 5QWs.

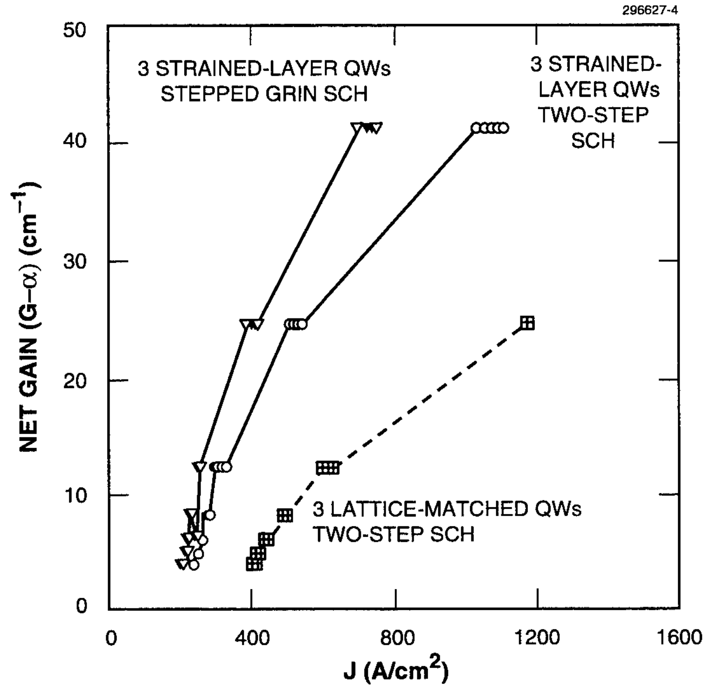

Figure 2-2. Net gain, G–α, vs current density J for three structures, all with 3QWs. The data on the right are from lattice-matched quantum wells and a two-step SCH structure. The data in the center are from biaxially compressed quantum wells with ≈ 1% strain and a two-step SCH structure. The data on the left are from the strained quantum wells and the stepped GRIN SCH structure.

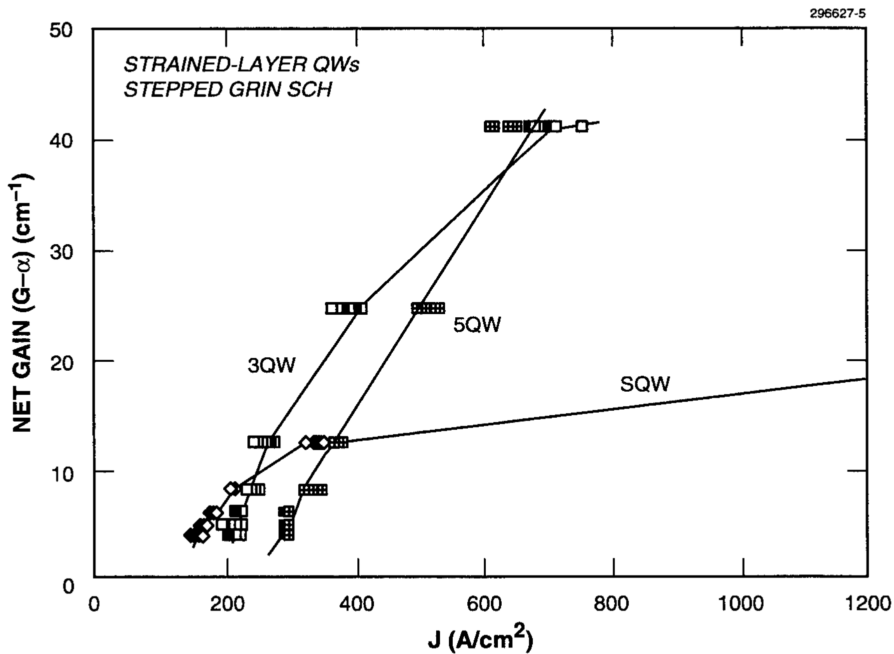

Figure 2-3. Net gain, G–α, vs current density J for stepped GRIN SCH with SQW, 3QWs, and 5QWs. In all cases the quantum wells are biaxially compressed with ≈ 1% strain.

Polarization insensitivity is important for some applications, but the TE-mode gain is higher than that of the TM mode in lattice-matched and biaxially compressed quantum-well devices. The most straightforward route to equal TE-TM gain is use of quantum wells with small, 0.3%, tensile strain, which places the uppermost heavy- and light-hole levels at the same energy. We have investigated 3QW and 5QW structures by this approach, using the strained ternary alloy, $In_{0.47}Ga_{0.53}As$, grown to 10.5-nm quantum-well widths. Equal TE-TM gain has indeed been realized. Relatively high J_t values are expected because of the degeneracy of hole levels, and we have observed J_t[3 mm] = 500 A/cm^2 and J_t[3 mm] = 650 A/cm^2 for 3QW and 5QW, respectively.

Summarized in Table 2-1 are representative values of J_t[3 mm], double-ended differential quantum efficiency at 0.5-mm cavity length η_d[0.5], usable net gain, and beam divergence for the various structures investigated. Although a search through the literature for results on comparable structures has not been made, our very competitive situation for the 1.3-μm devices leads us to believe that these 1.5-μm results are also of the highest quality. The materials have the excellent spatial uniformity that is important for large-area devices such as tapered amplifiers and oscillators [4]. Results from this variety of structures illustrate the trade-offs in device characteristics that are possible from variations in number and strain of the quantum wells and dimensions of the optical-confinement region.

S. H. Groves J. P. Donnelly
A. Napoleone R. J. Bailey

TABLE 2-1

Summary of Broad-Area Laser Properties for Various Structures

Description	J_t[3 mm] (A/cm^2)	η[0.5 mm] (%)	Net Gain (cm^{-1})	Divergence
3QW ($\partial a/a \approx 0$), two-step SCH	400	65	40 at 1.5 kA/cm^2	—
3QW ($\partial a/a \approx 1\%$), two-step SCH	200	80	40 at 1.0 kA/cm^2	—
3QW ($\partial a/a \approx 1\%$), stepped GRIN SCH	180	81	40 at 0.7 kA/cm^2	39°
Same, but reduced divergence	270	68	25 at 0.7 kA/cm^2	32°
SQW ($\partial a/a \approx 1\%$), stepped GRIN SCH	150	80	13 at 0.35 kA/cm^2	37°
5QW ($\partial a/a \approx 1\%$), stepped GRIN SCH	290	74	40 at 0.6 kA/cm^2	40°
Same, but reduced divergence	390	72	40 at 1.1 kA/cm^2	32°
Polarization insensitive:				
3QW ($\partial a/a \approx -0.3\%$), stepped GRIN SCH	500	62	40 at 3.3 kA/cm^2	—
5QW ($\partial a/a \approx -0.3\%$), stepped GRIN SCH	650	50	40 at 2.2 kA/cm^2	—

2.2 USE OF PROTON BOMBARDMENT TO REDUCE THE EFFECTS OF PHOTOGENERATED FREE CARRIERS IN PASSIVE-WAVEGUIDE OPTICAL FREQUENCY CONVERTERS

Previously, we have reported results on frequency (wavelength) converters based on four-wave mixing (FWM) that operate in the 1.5-μm-wavelength regime [5],[6]. These devices utilize the near-band-edge enhancement in the third-order nonlinearity in passive InGaAsP/InP quantum-well waveguides. The accumulation of photogenerated free carriers has been identified as a limitation on conversion efficiency of these frequency converters. Experiments with proton bombardment indicate that this technique has the potential to minimize these free-carrier effects.

In SQW devices, conversion efficiencies of ≥ -10 dB were observed during low-average-power pulsed operation. However, conversion efficiencies during CW operation were limited to ≤ -20 dB. A measurement of CW pump transmission vs pump power indicated a CW power-dependent loss that is greater than that expected from two-photon absorption. Since this phenomenological loss was observed under CW pump conditions, but not under short-pulse low-average-power conditions, a possible explanation is additional free-carrier loss due to the accumulation of photogenerated carriers under high-average-power operating conditions. Two measurements were done to test this hypothesis. In the first, the transmission of a low-power probe beam vs wavelength was measured with and without the presence of a high-power 1.55-μm pump beam. In the second, transient transmission was measured at the beginning of a long fast-risetime pulse. The results of these measurements supported the hypothesis that the enhanced absorption at high CW pump powers is due to the accumulation of photogenerated free carriers and not thermal effects.

In addition to fundamental absorption, two-photon absorption is a major contributor to the photogeneration of carriers. Accumulation of photogenerated free carriers is therefore expected to be a potential problem in the passive-waveguide sections of any monolithically integrated optical circuits operating with high average powers at wavelengths greater than half the bandgap. Since these carriers accumulate on a carrier-lifetime scale ($\approx$ 5–10 ns), it should be possible to eliminate or minimize photogenerated free-carrier effects by reducing carrier lifetime. This lifetime reduction must be accomplished without broadening the bandedge or increasing loss, both of which would have deleterious effects on FWM conversion efficiency.

Measurements of the relative transmission of the pump vs its power for an 8.5-mm-long SQW device are shown in Figure 2-4(a). Also shown are the calculated relative transmissions including the effects of two-photon absorption and additional loss due to the accumulation of photogenerated free carriers for several different carrier lifetimes. A wavelength-independent two-photon absorption coefficient of 46 cm/GW, which is consistent with high-power pulsed measurements made on these devices, was used in the calculations. The fundamental linear absorption coefficient was taken as the measured modal loss at the wavelength of interest minus the waveguide's parasitic losses, i.e., the asymptotic loss at long wavelengths. The net excess free-carrier loss α_{AFC} due to the accumulation of free carriers (electrons and holes with $n = p = N$) was taken as 2×10^{-17} cm$^2 \times N$ or $\alpha_{AFC} \approx 2$ cm^{-1} for $N = n = p = 10^{17}$ cm^{-3}. The $\tau = 0$ ns curve represents the loss expected from two-photon absorption alone. The experimental data agree fairly well with the $\tau = 10$ ns calculated curve, and it appears that reductions in lifetime of 1–2 orders of magnitude would minimize photogenerated free-carrier effects.

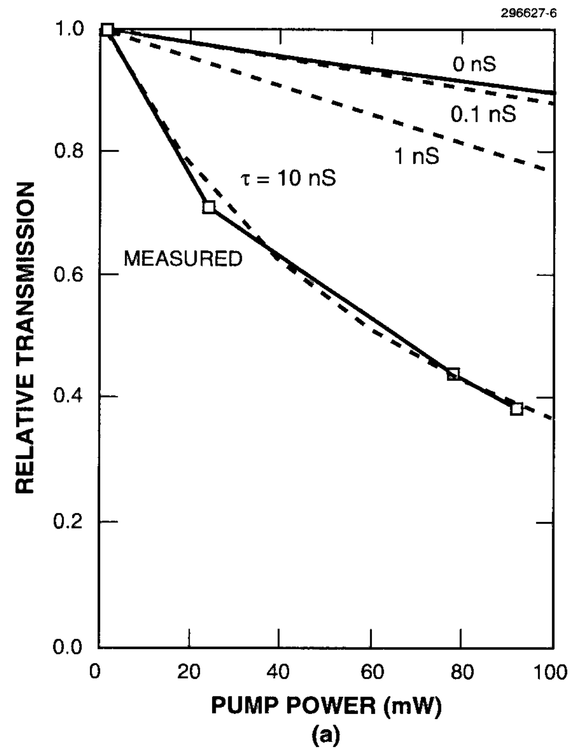

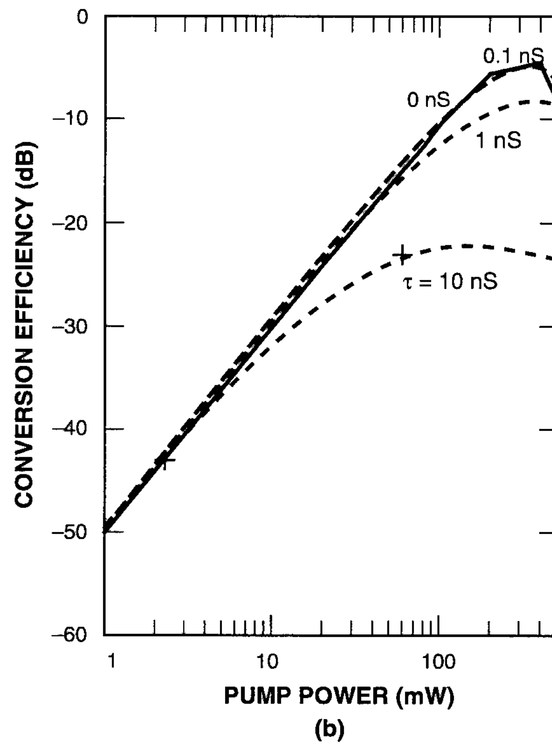

Figure 2-4. Response of SQW ridge waveguides: (a) experimental (squares) and calculated (dashed lines) relative pump transmission vs pump power, and (b) experimental (plus signs) and calculated (dashed lines) four-wave mixing conversion efficiency vs pump power. In (a) and (b), the $\tau = 0$ ns curves represent the results expected from two-photon absorption alone.

Calculated and measured conversion efficiencies vs pump power are shown in Figure 2-4(b). The conversion efficiencies including two-photon absorption and photogenerated free-carrier effects were calculated using the $|\chi^{(3)}|$ value determined from the low-power CW results. As with the pump-transmission data, the conversion efficiency data agree fairly well with the curves calculated using a carrier lifetime of $\tau = 10$ ns. The calculated curves also indicate that reductions in lifetime of 1–2 orders of magnitude should minimize photogenerated free-carrier effects for CW pump powers over 100 mW, which, as is shown later, should be adequate for obtaining conversion efficiencies of ≥ -10 dB over the entire erbium-doped fiber amplifier band in multiple-quantum-well devices.

One technique that is useful for reducing carrier lifetime is proton bombardment [7]. Proton bombardment, however, can increase optical loss [8] and possibly degrade the bandedge sharpness. We have therefore investigated the use of low-dose proton bombardment to see if it is possible to sufficiently reduce lifetime without introducing unacceptable loss or degradation in the sharpness of the bandedge. Since we are using ridge waveguide structures [5]–[6], a proton-bombardment schedule with a dose of N protons/cm^2 at 290 keV and $N/3$ at 90 keV was chosen. The dose at 290 keV maximizes the proton effects in the waveguide region under the ridge, while the 90-keV dose maximizes the effects outside the ridge region. In initial experiments, values of N between 3×10^{11} and 3×10^{12} cm^{-2} were investigated. As a simple way of evaluating the effects of the proton bombardment, low-temperature photoluminescence was used to determine both decreases in carrier lifetimes and increases in linewidth. Fabry-Perot loss measurements at a wavelength ≥ 40 nm below the bandedge were then carried out to determine the effects of the proton bombardment on waveguide loss.

The low-temperature photoluminescence spectra of SQW frequency-converter samples bombarded with proton schedules with $N = 3 \times 10^{11}$, 1×10^{12}, and 3×10^{12} cm^{-2} are shown in Figure 2-5 and compared to that of an unbombarded or control sample. Details of the device structure are given in Refs. 5 and 6. As compared to the unbombarded sample, the photoluminescence peak intensity is reduced by a factor greater than 10 times in the sample bombarded with the $N = 3 \times 10^{11}$ cm^{-2} proton schedule and by a factor greater than 100 times in the sample bombarded with the $N = 1 \times 10^{12}$ cm^{-2} proton schedule. These results indicate decreases in carrier lifetime over 10 and 100, respectively. For these two doses, the luminescence peak is at the same wavelength as the control and there are no indications of linewidth broadening. The peak intensity is down by ≈ 1000 times in the sample bombarded with the $N = 3 \times 10^{12}$ cm^{-2} proton schedule, but the low signal level makes it difficult to determine if there is appreciable linewidth broadening. Similar photoluminescence results were obtained on 3QW frequency-converter material.

Results of waveguide Fabry-Perot loss measurements on unbombarded and bombarded waveguide devices are shown in Figure 2-6. At 1.55 μm, the waveguide loss in the SQW and in one of the 3QW nonbombarded samples were on the order of 0.25–0.35 cm^{-1}. The other 3QW nonbombarded sample had loss in the 0.55–0.65 cm^{-1} range. Increases in loss for samples bombarded with $N = 3 \times 10^{11}$ and 1×10^{12} cm^{-2} proton schedules were typically < 0.1 cm^{-1} and were often within the scatter in the data on unbombarded samples. Even for devices bombarded with the $N = 3 \times 10^{12}$ cm^{-2} proton schedule, the increase in loss is < 0.2 cm^{-1}. Results on 5QW devices (not shown) are similar to those found on SQW and 3QW devices. These results indicate that low-dose proton bombardment could be an attractive technique for eliminating or minimizing the effects of accumulating free carriers in passive optical waveguides. A more definitive verification of this technique will be actual measurements under high-

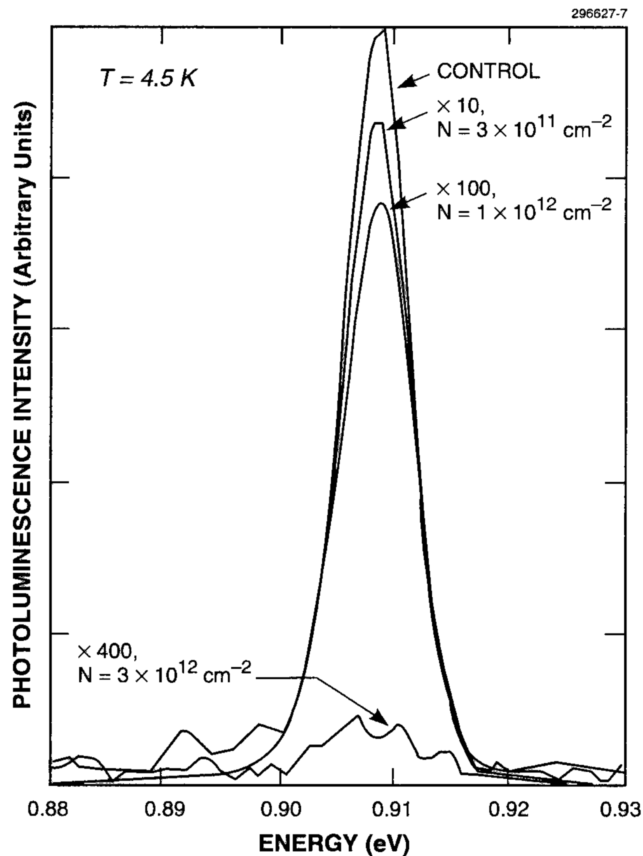

Figure 2-5. Low-temperature photoluminescence spectra of unbombarded and bombarded SQW wavelength-converter samples.

average-power operating conditions. To this end, SQW, 3QW, and 5QW control and proton-bombarded devices are being antireflection coated so high-power CW transmission and FWM experiments can be performed.

As an indication of the CW conversion efficiencies that should be achievable without the deleterious effects associated with photogenerated free carriers, we have calculated the conversion efficiency vs pump power at 20–70 nm below the bandedge for SQW and 5QW devices using $\chi^{(3)}$ and loss values vs wavelength obtained from low-power measurements on our initial SQW devices. The calculations are for wavelength shifts where dispersion is not a consideration. For multiple-quantum-well devices, we assumed the near-bandedge enhancement in $\chi^{(3)}$ scaled with the number of quantum wells. The loss at each wavelength was taken as $\alpha = \mathrm{NQW}\ (\alpha_{\mathrm{SQW}} - \alpha_{\mathrm{parasitic}}) + \alpha_{\mathrm{parasitic}}$, where α_{SQW} is the loss vs wavelength measured at low powers on the SQW devices and $\alpha_{\mathrm{parasitic}}$ is the waveguide parasitic loss not associated with the quantum wells, which was taken as the loss obtained by extrapolating the measured loss to long wavelengths. Figure 2-7 shows the results of the calculation for SQW and 5QW devices at

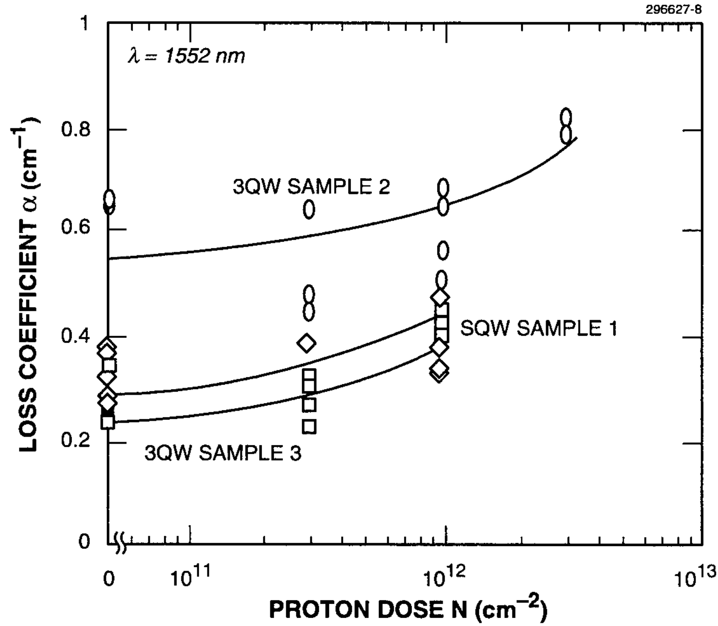

Figure 2-6. Results of Fabry-Perot loss measurements on unbombarded and proton-bombarded SQW and 3QW wavelength-conversion samples.

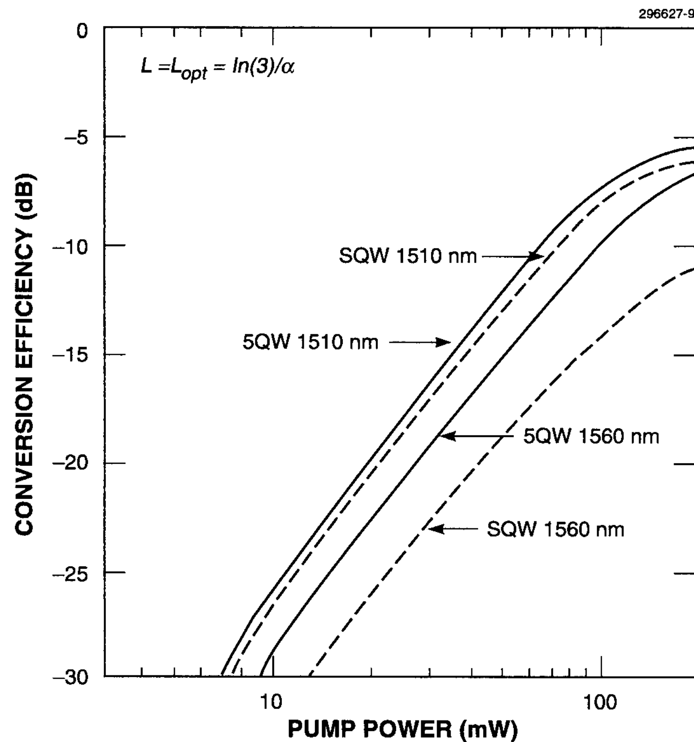

Figure 2-7. Projected CW conversion efficiency vs pump power of SQW and 5QW devices assuming elimination of excess loss due to accumulation of photogenerated free carriers. The parameters used in the calculation are based on $\chi^{(3)}$ and loss values obtained from low-power measurements on our initial SQW devices.

1510 and 1560 nm, which are 20 and 70 nm below the bandedge, respectively. The device length is assumed optimum for each wavelength. Separate calculations indicate that device length is not critical and that the actual device length can vary over a considerable range with only small reduction in conversion efficiency, making it possible to obtain near-optimum performance over a wide wavelength range in a single device. With 5QWs, both $\chi^{(3)}$ and the loss are dominated by the quantum wells even far from the bandedge, while with SQWs, parasitics play a large part in these parameters far from the bandedge. The 5QW projected conversion efficiencies are therefore substantially higher than those of the SQW device at 1560 nm. Closer to the bandedge, the difference between the 5QW and SQW conversion efficiencies is much smaller, since in this region the SQW device parameters are also dominated by the quantum-well parameters. As shown in the figure, elimination of photogenerated free-carrier effects should allow CW or high average conversion efficiencies of –10 dB at pump power levels < 100 mW over a wide wavelength range.

J. P. Donnelly
S. H. Groves
H. Q. Le
E. A. Swanson
R. J. Bailey
R. E. Reeder
A. Napoleone
J. W. Chludzinski
A. Darwish
E. R. Thoen
E. P. Ippen

2.3 MICROWAVE ANALOG OPTICAL LINKS USING SUBOCTAVE LINEARIZED MODULATORS

Optical analog links are useful in a variety of microwave application areas such as radar, satellite communications, and the new personal communication system network. Many of these applications require high third-order intermodulation-free dynamic range, but have bandwidths less than an octave, so second-order distortion is not important. We have developed a linearized modulator optimized for this type of application [9].

The linearized modulator consists of two standard Mach-Zehnder interferometric modulators (MZs) in series, as shown in Figure 2-8. (The device of Skeie and Johnson [10] is similar, but it minimizes both second- and third-order distortion by using reduced extinction on one modulator, which leads to more complexity and about a 6-dB noise figure penalty.) The RF input power is split between the two modulators to give the second MZ a modulation depth r compared to the first (the relative RF phase at the second modulator must be 0°). Three parameters control the transfer function of this modulator: r and the modulator phase bias points ϕ_1 and ϕ_2, which are set by the dc biases. The one constraint for linearization is that the third-order distortion must be minimized. Therefore, two parameters (r and ϕ_1, for example) can be chosen to reduce average detector current, which reduces the intensity noise and shot

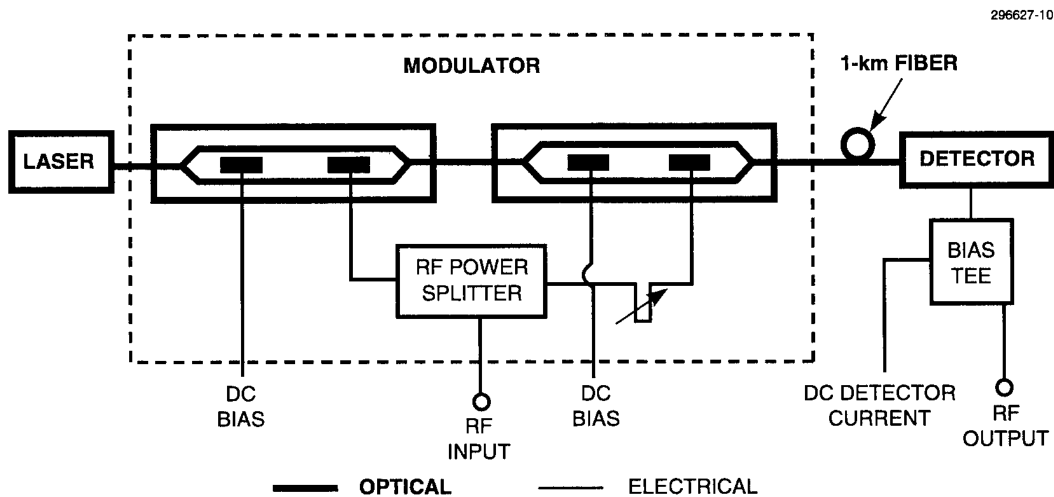

Figure 2-8. Configuration of experimental links which employ two Mach-Zehnder modulators in series.

noise at the link output while maintaining link gain. The third parameter (ϕ_2 here) must be carefully controlled to maintain minimum third-order distortion. Errors in r and ϕ_1 can be compensated by adjusting ϕ_2, so only a single bias point needs to be controlled. (Reference 9 describes the modulator operation in detail.) The series MZ modulator can be linearized at any frequency where the modulators operate; the tolerances on physical dimensions to keep the RF phase at the second modulator near 0° just become tighter as the frequency rises.

Our link experiments were accomplished by forming a series MZ out of two discrete single MZs, as shown in Figure 2-8. The electrical phase at the second modulator was set to 0° for all frequencies by setting the cable length to the second modulator so that the electrical time delay from the RF input to the second modulator via the cable was the same as the electrical time delay from the RF input to the first modulator plus the optical time delay from the first to the second modulator.

The three links we measured in these experiments are summarized in Table 2-2. The maximum detector current was the value measured with both modulators biased for maximum transmission. The average detector current is the dc photocurrent at the operating bias point.

Two different dynamic range numbers are shown in Table 2-2. The dynamic range at 1-MHz noise bandwidth is the fundamental-to-noise ratio at the point where the intermodulation signals are just equal to the noise level for a 1-MHz noise bandwidth. The normalized dynamic range in dB-$\mathrm{Hz}^{4/5}$ is obtained by calculating the output third-order intercept point (IP3) from the portion of the intermodulation signal-vs-power curve that has fifth-degree slope and then calculating the DR from

$$DR = \left[\frac{\mathrm{IP3}}{GFkT} \right]^{4/5} , \tag{2.1}$$

TABLE 2-2

Optical Link Performance

Center Frequency (MHz)	V_π (V)	Laser Power (mW)	Optical Loss (dB)	Detector Current Maximum (mA)	Detector Current Average (mA)	RF Gain (dB)	Noise Figure (dB)	Dynamic Range: 1-MHz Noise Bandwidth (dB)	Dynamic Range: Normalized (dB-Hz$^{4/5}$)
500	2.7	90	11	7.1	0.94	−10.8	27.7	88	133
900	5.6	90	11	5.3	0.43	−30.6	42.6	76	124
2000	6.0	100	7.0	10.3	1.64	−28.2	35.0	75	116 dB-Hz$^{2/3}$

where G is the RF gain, F is the noise figure, and kT is the thermal noise at 290 K in a 1-Hz bandwidth. The normalized dynamic range is useful when one is interested in RF power levels and bias conditions where the intermodulation slope is uniformly 5. However, the dynamic range at 1-MHz noise bandwidth is a more useful number if one is interested in noise bandwidths near 1 MHz, because the intermodulation slope can deviate from 5, especially at small modulation depths.

The typical active bias control method is to apply pilot tones and then minimize the unwanted outputs; here ϕ_1 is uncontrolled (passive stabilization can hold it to ± 5° over a 100°C temperature range) and the third-order distortion is minimized by controlling ϕ_2. The dynamic range is fairly tolerant to bias errors: even a ± 2° error (± 0.5° is normally achievable) preserves significant dynamic range advantage over the standard single MZ modulator.

The 500-MHz link [11] had no problems and demonstrated the full dynamic range capability of this type of modulator. The link used commercial modulators with good response at 500 MHz. The operating condition was $r = 1$, $\phi_1 \approx 90°$, and $\phi_2 \approx 118°$. This value for ϕ_2 agrees closely with the theoretical prediction of the ϕ_2 required for linearization with $r = 1$, $\phi_1 = 90°$. The detector had a passive resonant-impedance-matching circuit (180-MHz bandwidth centered at 470 MHz) so its effective load resistance was 425 Ω, which added 9 dB to the link RF gain. This elevated the shot noise output power so it far exceeded the receiver thermal noise power at the 0.94-mA dc photocurrent level. In a two-tone test at 530 MHz, the dynamic range was 88 dB in a 1-MHz noise bandwidth, which is slightly larger than the 85 dB obtained by using Equation (2.1) and the measured IP3 of +9 dBm. The noise figure of 27.7 dB was only 0.4 dB higher than a link using a standard single MZ with the same laser power, optical loss, and modulator response [9]. The noise figure could be further reduced with a reduction in gain but no dynamic range penalty by changing the operating point. For $r = 2.88$, $\phi_1 \approx 60°$, and $\phi_2 \approx 155°$, we measured a noise figure of 26.3 dB, which was lower than that of the comparison single-MZ link.

The 900-MHz link showed the expected linearization, but it had an unexpectedly high noise figure. The high noise figure was due to the low response of the commercial modulators at 900 MHz, the lack of detector impedance matching, and the inadvertent connection of an extraneous noise source to the link input during the noise-figure measurement. The linearization worked correctly, though, as can be seen by the 40-dB improvement in intermodulation suppression relative to a standard MZ shown in Figure 2-9(a). Even with the excessively high output noise, the normalized dynamic range was 124 dB-Hz$^{4/5}$ (if shot noise were the only output noise source, the output noise would have been 10 dB lower and the dynamic range would have been 132 dB-Hz$^{4/5}$). At 1-MHz noise bandwidth, the fifth-degree slope for the intermodulation-vs-input power held down to below the noise floor, giving a dynamic range of 76 dB. At the cellular-telephone channel bandwidth of 30 kHz, the slope started to deviate from fifth degree before reaching the noise floor, giving a dynamic range of 86 dB. This is still 6 dB better than the generally used base-station specification.

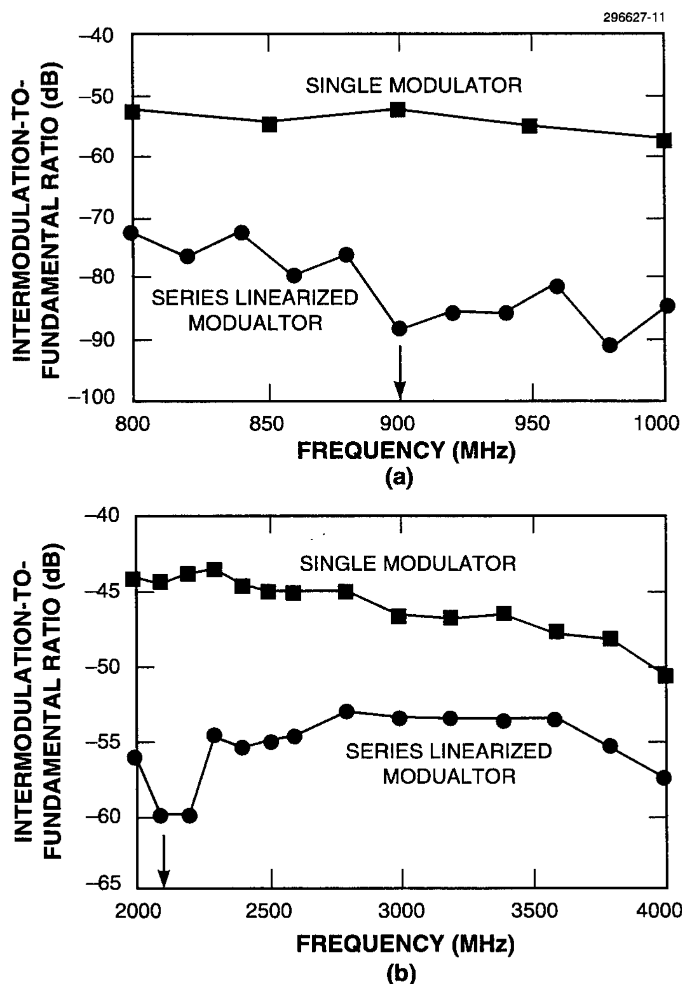

Figure 2-9. Third-order intermodulation suppression vs frequency: (a) 900-MHz link, modulation depth m(V) = 0.13 per frequency at 900 MHz, and (b) 2-GHz link, m(V) = 0.27 per frequency at 2.1 GHz. The modulator bias points were set for minimum two-tone intermodulation at the frequencies indicated by the arrows; then the two frequencies (1-MHz separation) were swept over the band to produce the plot.

A 2- to 4-GHz link [12] showed better linearity than a comparison link using a standard MZ, but did not show the ideal linearization of the two lower-frequency links. The intermodulation-vs-input power slope was third degree at all but the highest modulation depths tested, and the bias point settings for best linearity deviated from those predicted by our theory. The source of this problem was optical reflections in the link. This link used a pair of older, laboratory-built traveling-wave modulators that had better frequency response and optical transmission than the commercial modulators, but did not have angled end faces to suppress optical reflections. The 4% optical reflection at each of the four fiber/waveguide joints seriously degraded the linearization because some light made multiple passes through the modulators. Despite this problem, the intermodulation products were reduced 15 dB below those of a standard MZ at a modulation depth of 0.27 per frequency in a two-tone measurement, as seen in Figure 2-9(b). The dynamic range of the link at 2 GHz was 75 dB with a 1-MHz bandwidth, and the normalized dynamic range was 116 dB-$Hz^{2/3}$, with only 1.6-mA average detector current.

We have demonstrated optical analog links at 500, 900, and 2000 MHz using linearized modulators at practical optical power levels that show up to 15-dB improvement in dynamic range over similar links with standard modulators. There is no fundamental noise figure or frequency response penalty for this type of linearization. A more complete summary of these experiments is available in Ref. 13.

G. E. Betts
F. J. O'Donnell

REFERENCES

1. Solid State Research Report, Lincoln Laboratory, MIT, 1994:1, p. 1.
2. Solid State Research Report, Lincoln Laboratory, MIT, 1994:2, p. 4.
3. S. C. Palmateer, S. H. Groves, J. W. Caunt, and D. L. Hovey, *J. Electron. Mater.* **18**, 645 (1989).
4. S. H. Groves, J. P. Donnelly, J. N. Walpole, J. D. Woodhouse, L. J. Missaggia, R. J. Bailey, and A. Napoleone, *IEEE Photon. Technol. Lett.* **6**, 1286 (1994).
5. Solid State Research Report, Lincoln Laboratory, MIT, 1996:3, p. 7.
6. J. P. Donnelly, H. Q. Le, E. A. Swanson, S. H. Groves, A. Darwish, and E. P. Ippen, *IEEE Photon. Technol. Lett.* **8**, 623 (1996).
7. A. G. Foyt, F. J. Leonberger, and R. C. Williamson, *Appl. Phys. Lett.* **40**, 447 (1982).
8. F. J. Leonberger, J. N. Walpole, and J. P. Donnelly, *IEEE J. Quantum Electron.* **QE-17**, 830 (1981).
9. G. E. Betts, *IEEE Trans. Microwave Theory Tech.* **42**, 2642 (1994).
10. H. Skeie and R. V. Johnson, *Proc. SPIE* **1583**, 153 (1991).
11. G. E. Betts and F. J. O'Donnell, *Proceedings of the IEEE Lasers and Electro-Optics Society* (IEEE, New York, 1994), p. 278.
12. G. E. Betts, *1995 Optical Fiber Communication Conference Technical Digest* (Optical Society of America, Washington, D.C., 1995), p. 243.
13. G. E. Betts and F. J. O'Donnell, *IEEE Photon. Technol. Lett.* **8**, 1273 (1996).

3. SUBMICROMETER TECHNOLOGY

3.1 NANOCHANNEL FABRICATION FOR CHEMICAL SENSORS

Although biochemical analysis techniques such as ion mass spectrometry, gas and liquid chromatography, pH meters, and capillary electrophoresis have been simplified by the inclusion of integrated circuit technology, the basic physical processes used to determine the chemical constituents have not changed. Furthermore, some biochemically active agents such as Pb, bromates, and amines are toxic below the limits of current instrument detectability.

We propose a new type of chemical sensor, the chemical charge-coupled device (CCD), which will be able to separate and concentrate ions in solution with high sensitivity. By using advanced integrated circuit techniques to fabricate structures on a size scale comparable to the Debye length in ionic solutions (2–200 nm), it should be possible to use the resulting high fields at the insulator-fluid interface to manipulate ions in solution according to their mobility. The ability to increase and also to control the ion concentration in a capillary channel by adjusting the potential of a single polysilicon control electrode has been demonstrated in the ionic liquid-channel field-effect transistor [1]. The new sensor will utilize sequenced multiple-gate structures to step ions in an electrolyte solution down the channel, as shown in Figure 3-1. Its structure and operation are analogous to that of the familiar electronic CCD used in imaging and signal processing applications. In the chemical CCD the ion concentration will ultimately be controlled by the interaction between the stepping frequency, the multiplicity of electrodes, and the ion diffusion coefficient. Initial calculations predict the ability to concentrate the ions of interest by several orders of magnitude. Once concentrated, these impurities can be detected by a change in electrical conductivity, a change in electric potential locally at the output end of the CCD, or by a fluorescence technique. Electrodes embedded at the end of the channel can detect the conductivity increase with a calculated detection limit of ~ 1000 ions. For a field-effect transistor having its drain and source in the same Si substrate containing the chemical CCD and with the electrolyte acting as the gate electrode, the calculated detection limit is 10–100 ions.

To manipulate ions in an electrolyte with CCD technology, the basic electronic CCD structure is modified by the addition of a counterelectrode, as shown schematically in Figure 3-1. This counterelectrode extends the full length of the device, defines the average potential in the channel, and is placed below the conventional CCD segmented electrodes on the top of the channel. The channel height is designed to be less than or equal to the Debye length in the electrolyte of interest. The Debye length, $D = (kT\varepsilon\varepsilon_o/Nq^2)^{1/2}$ (cm) is the $1/e$ distance over which the electric field can penetrate into an electrolytic solution, where k is Boltzmann's constant (1.38×10^{-23} J K^{-1}), T is the temperature (K), ε is the dielectric constant of the fluid, ε_o is the permittivity of vacuum (8.85×10^{-14} F cm^{-1}), N is the ion concentration (cm^{-3}), and q is the charge on an ion (a multiple of 1.6×10^{-19} C). The electrolyte Debye length varies from 2 to 200 nm in water solutions depending upon the electrolyte dielectric constant and the ion concentration. The electrodes are insulated from the electrolyte-filled channel by a thin dielectric layer. In the conventional silicon-based CCD, the Si-SiO_2 interface must be of device quality to control the electrons in the semiconductor. In a similar fashion, the insulator-electrolyte interface in the chemical CCD must be of device quality to control the ions in solution. Si_3N_4-water and Si_3N_4-glycerine solutions were found to be of device quality [1].

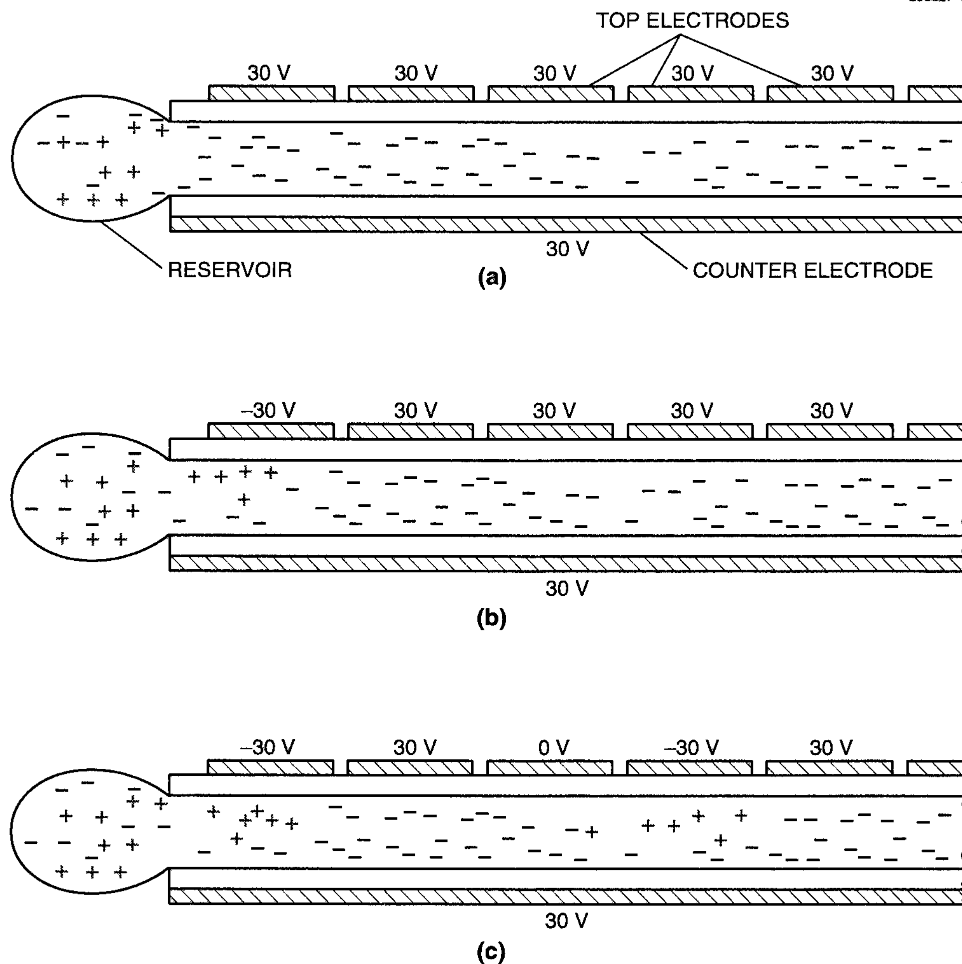

Figure 3-1. Schematic diagram of a chemical charge-coupled device (CCD): (a) distribution of ions in channel for all electrodes being positively charged with respect to the electrolyte reservoir, (b) ion distribution when first electrode at reservoir is negatively charged, and (c) ion distribution after positive ion packet is stepped four electrodes to right. A new positive ion packet is being formed under the first electrode.

By applying a positive bias to all the electrodes, most of the positively charged ions can be eliminated from the channel, as in Figure 3-1(a). A negative bias applied to the electrode next to the reservoir will cause a packet of positively charged ions to form under that electrode, as in Figure 3-1(b). These ions can then be moved through the channel by negatively biasing consecutive electrodes, producing an ion current to the right, as shown in Figure 3-1(c). Similarly, ion packets can be moved to the left with appropriate biasing and voltage changes. Packets of negative ions can also be formed by changing the sign of the applied voltages. If the voltage changes occur too fast, for example, stepping frequencies > 1–10 kHz, some of the ions in each packet will be left behind and later will be localized in a trailing packet.

Once a packet of positive ions is formed in the channel, the ionic constituents can be separated according to their diffusion coefficients. This results because ions with low diffusion coefficients will take longer to move between the regions controlled by adjacent electrodes than ions with higher diffusion coefficients. If the stepping frequency, defined as the number of voltage changes per second, does not allow sufficient time for a given ion constituent to diffuse between adjacent electrode regions, then the ion flux or current through the channel for that constituent will be reduced. Figure 3-2 shows a comparison of the ion current per voltage step for two constituents with substantially different diffusion coefficients: Li^+ with 1.03×10^{-5} cm^2 s^{-1}, and H^+ with 9.07×10^{-5} cm^2 s^{-1}.

For the CCD geometry modeled here, stepping frequencies near 1 kHz will have a substantial H^+ current but a reduced Li^+ current. At still higher frequencies (> 10 kHz) even the H^+ current will decrease. This effect is shown in Figure 3-2, which displays the ion current for several frequencies as a function of the diffusion coefficient. By operating the CCD repeatedly at several different frequencies, it should be possible to select ion constituents within a narrow band of diffusion coefficients. If the number of stepping periods for each process is small in comparison to the number of CCD electrodes, then the effective ion current is the sum of the currents produced by the different frequencies. Since the channel can have several thousand electrodes the ultimate concentration of the target ions can be many orders of magnitude above that at the reservoir. Figure 3-3 shows the simulated ion concentration ratio as a function of the diffusion coefficient for a 600-electrode CCD. Such a CCD would be 600 μm long, with 10 parallel channels 0.1 μm high and 10 μm wide having an electrolyte volume of 6×10^{-9} cm^{-3}. The predicted ability to concentrate ions by 10^{14} assumes a constant Debye length. For an actual device, the Debye length will decrease by the square root of the ion concentration, so such a large increase in concentration will not be obtained. However, this limitation will occur at ion concentrations well above the detection limit.

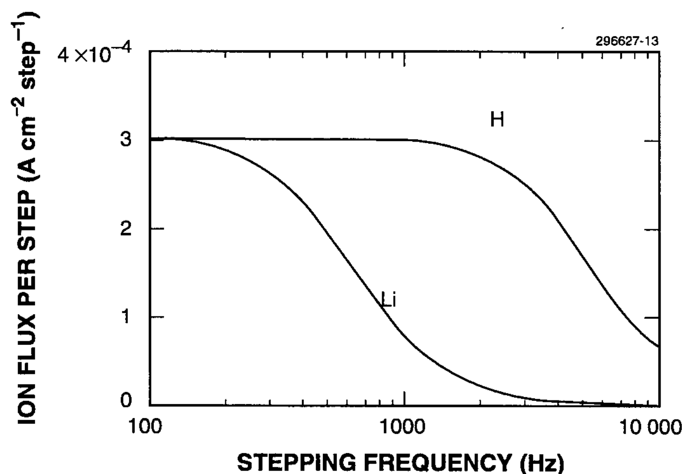

Figure 3-2. Simulated ion current per step of Li^+ and H^+ ions through chemical CCD as function of stepping frequency. The CCD electrodes were assumed to be on 1-μm centers for the theoretical results shown here.

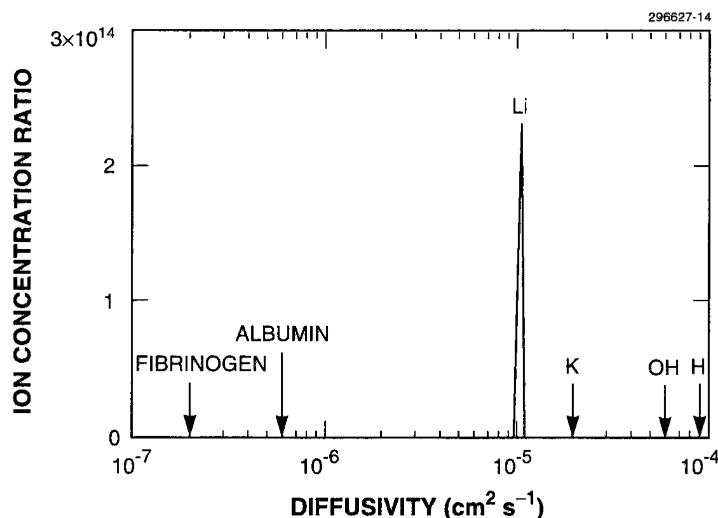

Figure 3-3. Predicted ability of chemical CCD to concentrate ions. The calculations assumed 1-μm-long CCD electrodes and three stepping frequencies of 100, 1000, and 1100 Hz. The concentration ratio is plotted as a function of diffusion coefficient. The diffusion constants of several ions in water are shown for comparison.

The fabrication of hollow dielectric channels several millimeters long and with height less than the Debye length (≤ 100 nm in the electrolyte of interest) is critical to the realization of the chemical CCD. A mask set has been designed and a 100-mm Si process implemented to fabricate Si_3N_4 capillary nanochannels with heights of 20, 50, and 100 nm; widths between 0.5 and 200 μm; and lengths up to 1 cm. Figure 3-4 shows an overview of the mask set and a cross section through a capillary channel. Thin films of SiO_2, Si_3N_4, amorphous Si, and poly Si are sequentially deposited and patterned to define channel and reservoir structures on an Si substrate. The sacrificial amorphous Si filling the channel is subsequently wet etched in tetramethylammonium hydroxide (TMAH) to form the microcapillary structures. A scanning electron micrograph of a 1-μm-wide, 100-nm-high channel is shown in Figure 3-5. The channel etch rate depends sensitively on the amorphous-Si film thickness and the patterned channel width, shown in Figure 3-6, and weakly on the temperature and strength of the etchant. Samples have been etched in 10–25% TMAH solutions (in water) and at temperatures from 23 to 90°C. Typical Si etching rates are between 25 and 37 μm/h depending on the width and height of the channel. Several interesting results are observed. The channel etching rates saturate with time as can be seen in Figure 3-5 for a 5-μm channel, where samples have been etched in excess of 80 h. The reduction in channel etch rate with increasing channel length is attributed to reduced fresh reactant concentration due to mass transport effects. In addition, although the etch rates of SiO_2 and Si_3N_4 in a 10% TMAH solution at 75°C are slow, ≤ 5 nm/h, at very long etch times the thin layers of dielectric are considerably thinned, imparting an upper limit of 3–5 mm to the practical channel length. As this will impact the interfacial quality of the dielectric-electrolyte interface, it is a topic of further study. Structural integrity is dependent

on channel width. Channels with widths > 30 μm collapse almost immediately after amorphous Si is etched; after 20 h the 20-μm-wide channels collapse; and at times > 50 h the 5- and 10-μm channels collapse. The dip in the center of the channel due to the collapse has been measured with both atomic force microscopy and stylus profilometry. The role of film stress in causing this condition is currently under investigation.

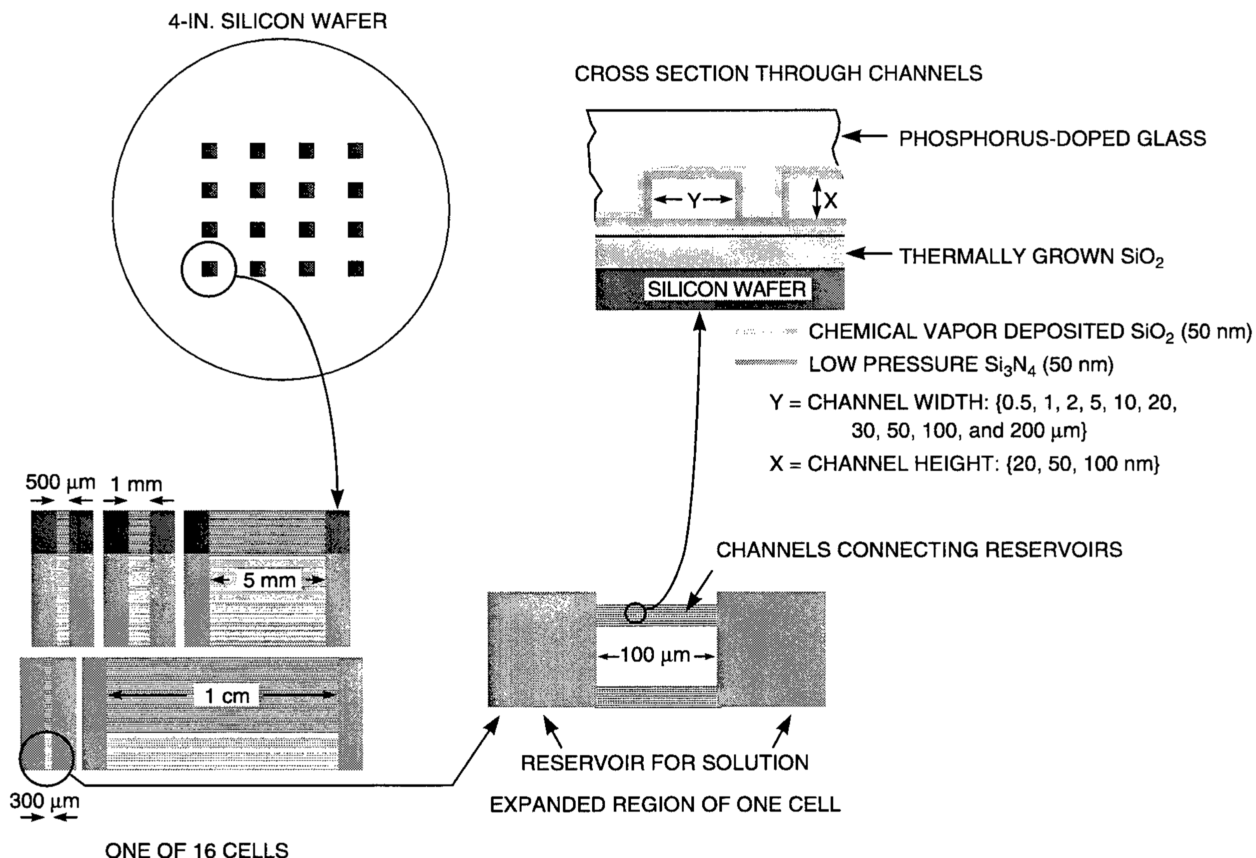

Figure 3-4. Overview of channel structure layout and schematic cross section of Si nanochannel.

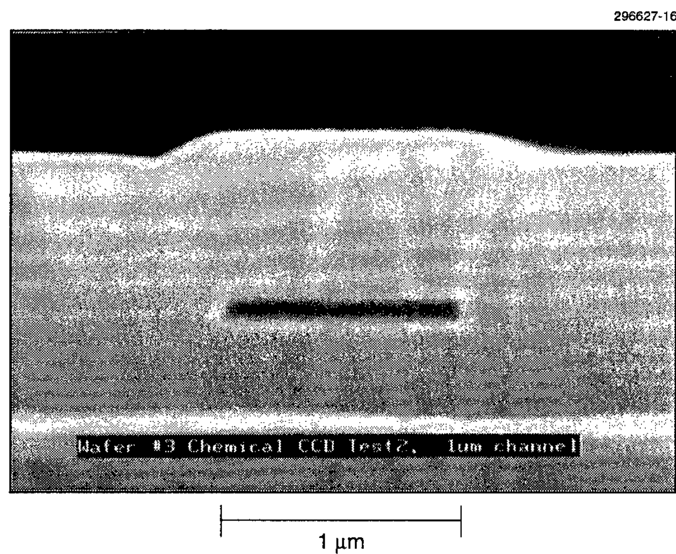

Figure 3-5. Scanning electron micrograph of channel fabricated in Si. This channel is 1 μm wide, 50 nm high, and > 1 mm in length.

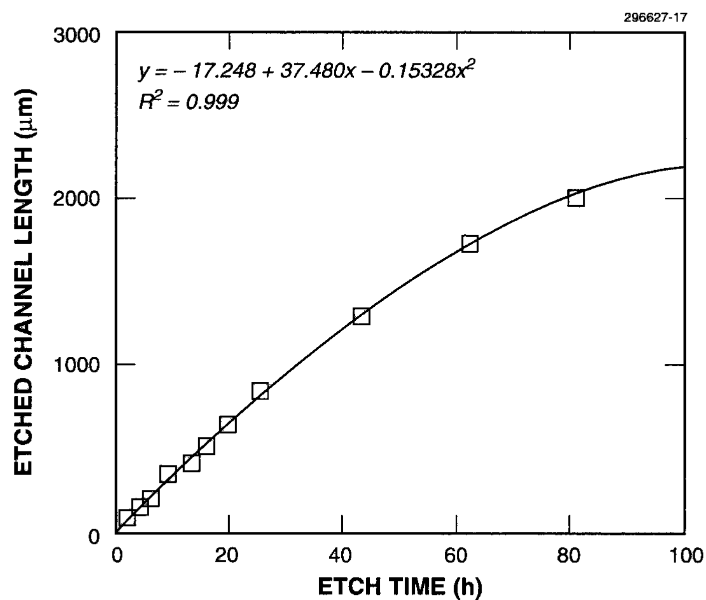

Figure 3-6. Graph of 5-μm-wide channels, 100 nm high, etched for up to 80 h.

These results demonstrate the capability of fabricating capillary nanochannels. Based on these observations we have designed a CCD mask set with channel widths of 10 μm and channel lengths up to 3 mm, and are preparing to fabricate chemical CCD devices on 150-mm-diam Si wafers.

M. B. Stern
M. W. Geis
J. E. Curtin

REFERENCE

1. S. A. Gajar and M. W. Geis, *J. Electrochem. Soc.* **139**, 2833 (1992).

4. HIGH SPEED ELECTRONICS

4.1 THICKNESS INHOMOGENEITY OF ELECTRONIC PROPERTIES OF GaN EPILAYERS

Previously, we have demonstrated [1] that hydride vapor phase epitaxy (HVPE) is capable of growing thick heteroepitaxial GaN films on sapphire substrates with greatly improved structural and electronic properties as compared to films grown by metallorganic vapor phase epitaxy or molecular beam epitaxy [2],[3]. Dislocation densities as low as ~ 5×10^7 cm^{-2} and room-temperature electron mobilities of ~ 900 cm^2/V s have been attained for ~ 75-μm-thick, unintentionally doped GaN films with an electron background of ~ 8×10^{16} cm^{-3} (300 K) [4],[5]. Characterization of Schottky diodes formed on HVPE-grown GaN films by deep-level transient spectroscopy (DLTS) revealed deep-level concentrations below 10^{16} cm^{-3} [6]. However, in the same films the presence of deep levels with thermal ionization energies in the range from 100 to 200 meV and concentrations as high as ~ 5×10^{18} cm^{-3} were derived from the temperature dependence of the electron concentration by Hall-effect measurements [6].

The above contradictory results motivated the present study. For the analysis of the Hall effect data, uniformity of the electronic properties throughout the film thickness is assumed. To investigate the electronic properties as a function of film thickness, a 13-μm-thick HVPE-grown GaN layer was characterized by variable-temperature Hall-effect measurements, capacitance-voltage (C-V) measurements, and DLTS. Subsequently, the film thickness was reduced to 7 and 1.2 μm by mechanical polishing and characterized by the same techniques at each of the thickness steps.

The GaN material used in this study was grown in a vertical HVPE reactor which is described in [5]. The nucleation of the GaN on *c*-plane sapphire substrates was enhanced by a GaCl pretreatment [4],[7]. The film was grown at 1050°C to a thickness of 13 μm with a growth rate of 13 μm/h.

The Hall-effect measurements were conducted in the temperature range between 80 and 500 K with a magnetic field of 17.4 kG. For the measurements, samples 5×5 mm^2 in size were cut from the wafers, and ohmic metal contacts were deposited in the Van der Pauw geometry.

Conventional C-V measurements were conducted to investigate the depth profile of the dopants below the surface of the GaN films. Schottky diodes were fabricated by evaporating Au through a shadow mask onto the surface of the GaN samples. The measurements were conducted with a 1-MHz, 10-mV test signal up to a reverse bias of ~ 20 V.

The Schottky diodes were also utilized to perform DLTS measurements in the temperature range between 75 and 475 K. The DLTS system employed in this study is described in [8]. The film thinning was accomplished by mechanical polishing. The final polish achieved an rms surface roughness of < 10.

Results from variable-temperature Hall-effect measurements are shown in Figure 4-1 (symbols). Figure 4-1(a) displays electron concentrations as a function of temperature for the as-grown film (d = 13 μm) and after thinning by mechanical polishing to thicknesses of 7 and 1.2 μm. The electron concentrations significantly increase with decreasing film thickness. Figure 4-1(b) shows the electron mobility as

a function of temperature for the three different film thicknesses. The electron mobility decreases with decreasing film thickness.

The experimental data for the original film thickness were analyzed using the charge neutrality condition [9], assuming two independent donors and acceptor compensation [solid line in Figure 4-1(a)]. The analysis yields a shallow donor with an activation energy (thermal ionization energy) of ~ 18 meV and a concentration of ~ 2×10^{17} cm^{-3}. The presence of a second donor is required to explain the high-temperature portion of the experimental Hall-effect data. The parameters for the second donor are ~ 180 meV and ~ 5×10^{17} cm^{-3} for the activation energy and concentration, respectively. The analysis assumes that these donors are uniformly distributed throughout the thickness of the HVPE film.

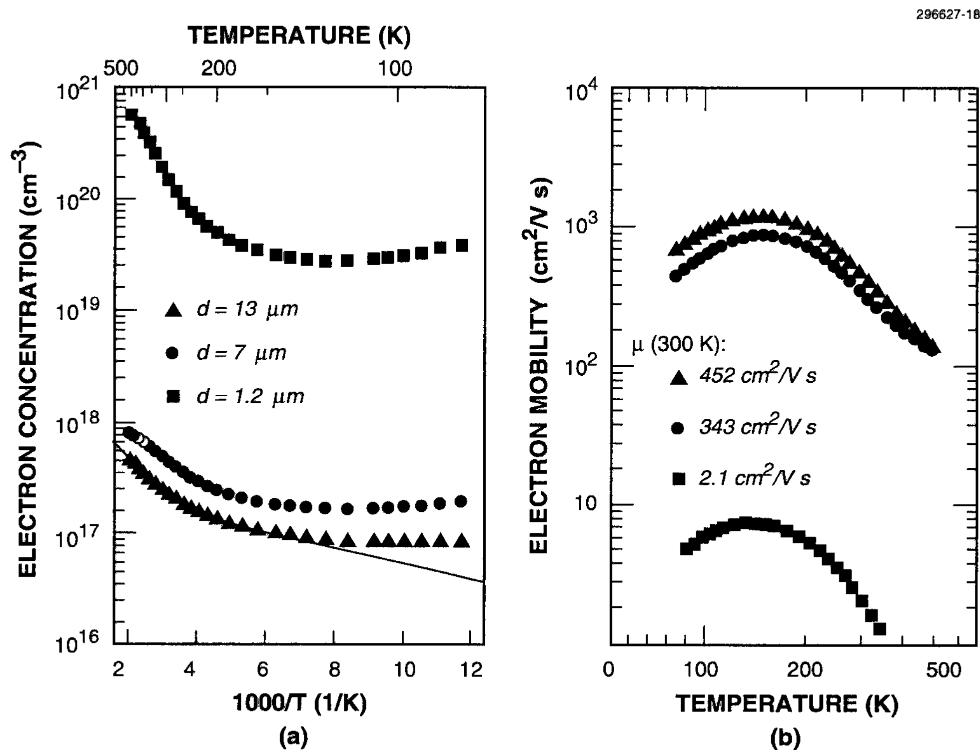

Figure 4-1. (a) Electron concentration vs reciprocal temperature and (b) electron mobility vs temperature for n-type GaN films grown by hydride vapor phase epitaxy (HVPE). Films are of three different thicknesses as determined from variable-temperature Hall-effect measurements.

Results from C-V measurements as a function of film thickness are shown in Figure 4-2. The effective donor ($N_D^+ - N_A$) concentrations depicted in Figure 4-2 are average concentrations derived from the depth profiles. As an example, the depth profile of $N_D^+ - N_A$ determined for a film thickness of 7 μm is shown in the inset of Figure 4-2. The C-V results indicate that $N_D^+ - N_A$ stays approximately constant from the original film thickness to a depth of ~ 1 μm away from the GaN/sapphire interface.

Results from DLTS are shown in Figure 4-3. Displayed is a DLTS spectrum measured for our HVPE-grown GaN material at the original film thickness (13 μm). The spectrum which was recorded for an instrumental emission rate of 46.2 s^{-1} reveals the presence of four discrete deep levels. They are labeled DLN_1, DLN_2, DLN_3, and DLN_4. For this particular sample, the deep-level DLN_2 appears only as a shoulder and, therefore, was not considered for analysis. The measurement was repeated after each polishing step; however, the spectra are not shown in Figure 4-3. The DLTS spectra were analyzed assuming a temperature-independent capture cross section. The defect parameters for DLN_1, DLN_3, and DLN_4 are depicted in Figure 4-3 as functions of film thickness. Activation energies for electron emission to the conduction band for DLN_1, DLN_3, and DLN_4 were determined to range from 0.23 to 0.25 cV, 0.59 to 0.63 cV, and 0.86 to 0.91 cV, respectively. The activation energies for the three deep levels only vary within the experimental uncertainties for the measurements at different sample thicknesses, indicating that each DLTS measurement detected the same deep levels. The concentrations of DLN_1 and DLN_3 also vary only within experimental uncertainties, showing that these deep levels are almost uniformly distributed within the investigational thickness range. An exception is DLN_4, for which the concentration is more than two times higher at a film thickness of 1.2 μm than at the original film thickness.

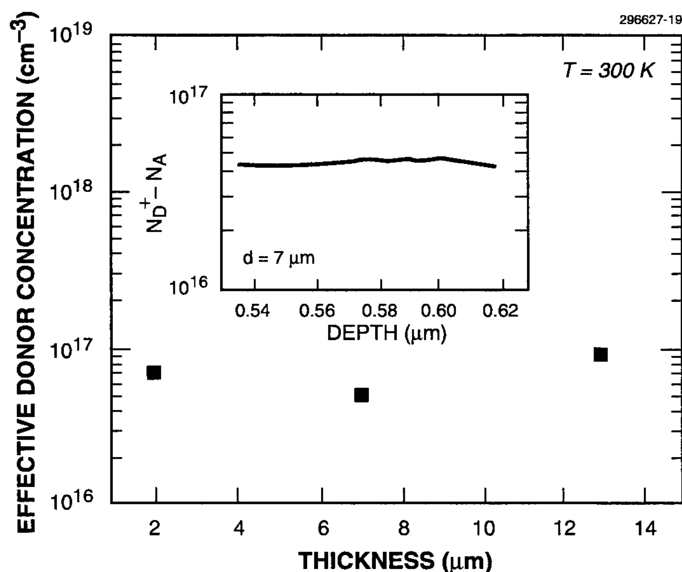

Figure 4-2. Net donor concentration ($N_D^+ - N_A$) for HVPE-grown n-type GaN as determined by capacitance-voltage measurements on Au Schottky diodes for three different film thicknesses. The inset demonstrates the net donor depth profile for a film thickness of 7 μm.

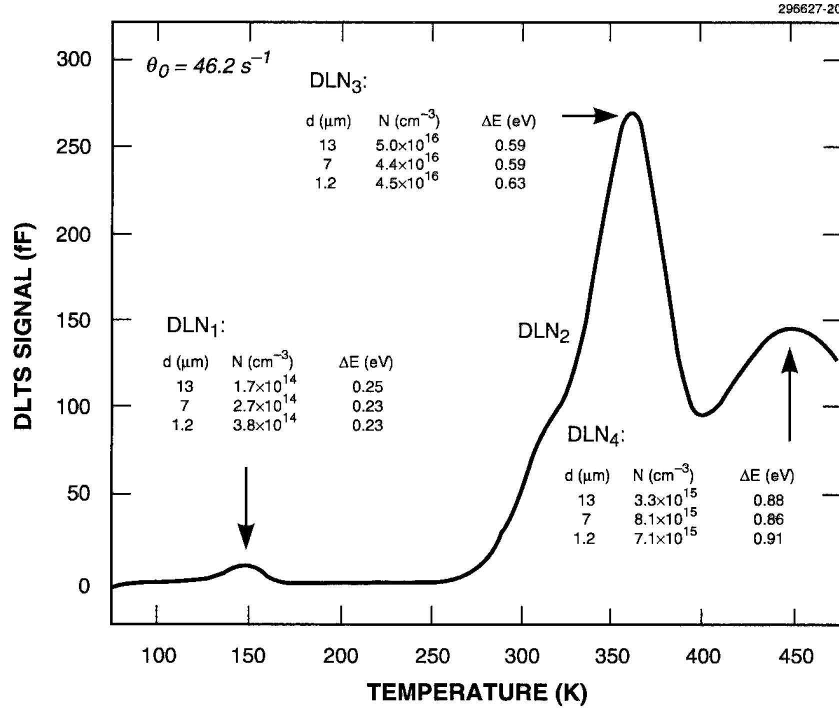

Figure 4-3. Deep-level transient spectroscopy spectrum for HVPE-grown n-type GaN (original film thickness). The peaks in the spectrum indicate the presence of discrete deep levels. The parameters (concentration N, and activation energy for electron emission to the conduction band, ΔE) for three deep levels are depicted for three different film thicknesses d.

The experimental data presented in this study demonstrate that shallow as well as deep levels are homogeneously distributed in the major portion of the 13-μm film. This is evident from C-V (Figure 4-2) and DLTS measurements (Figure 4-3), respectively, which were conducted for three different film thicknesses. The DLTS measurements also show that the concentrations of detected deep levels do not exceed concentrations of ~ 10^{16} cm^{-3}. However, Hall measurements indicate a significant increase in electron concentration with decreasing film thickness as well as the presence of a deep donor level in concentrations above ~ 10^{18} cm^{-3}. This behavior may be explained by the presence of a thin, highly conductive GaN layer close to the GaN/sapphire interface. For depth inhomogeneities, the Hall-effect measurements yield an effective areal density of free electrons $n_{s,\mathrm{eff}}$ and an effective Hall mobility μ_{eff} [10]. For a two-layer model, the product $n_{s,\mathrm{eff}}/\mu_{\mathrm{eff}}$ is given by

$$n_{s,\mathrm{eff}}\mu_{\mathrm{eff}} = n_i \mu_i d_i + n\mu(d - d_i) \ , \qquad (4.1)$$

where d_i is the thickness of the interface layer and n, μ, and n_i, μ_i are the electron concentrations and mobilities of the GaN film (without interface layer) and the interface layer, respectively. The presence of an ~ 200-nm-thick, highly defective interface layer was detected from transmission electron microscopy for the HVPE film investigated in the present study [5]. Under the assumption that this interface layer is responsible for the observed electrical phenomena, a lower limit ($\mu_i = \mu$) of the shallow donor and the deep-level concentration in the interface layer can be estimated with Equation (4.1). With d_i ~ 200 nm, the shallow donor concentration in the interface layer becomes $> 5 \times 10^{19}$ cm^{-3} and the deep-level concentration becomes $> 2 \times 10^{20}$ cm^{-3}. The atomic concentration of potential donors (O, Si) in the interface layer as determined by secondary ion mass spectroscopy cannot account for the estimated shallow donor concentration. Thus, for both shallow donors and deep levels the responsibility of native defects is implied.

W. Götz *
R. J. Molnar

*Author not at Lincoln Laboratory.

REFERENCES

1. R. J. Molnar, W. Götz, L. T. Romano, and N. M. Johnson, *Electrochem. Soc. Proc.* **96-11**, 212 (1996).
2. S. N. Mohammad, A. A. Salvador, and H. Morkoç, *Proc. IEEE* **83**, 1306 (1995).
3. S. D. Lester, F. A. Ponce, M. G. Craford, and D. A. Steigerwald, *Appl. Phys. Lett.* **66**, 1249 (1995).
4. R. J. Molnar, P. Maki, R. Aggarwal, Z. L. Liau, E. R. Brown, I. Melngailis, W. Götz, L. T. Romano, and N. M. Johnson, *Mater. Res. Soc. Symp. Proc.* **423**, 221 (1996).
5. R. J. Molnar, to be published in *J. Cryst. Growth.*
6. W. Götz, L. T. Romano, B. S. Krusor, and N. M. Johnson, *Appl. Phys. Lett.* **69**, 242 (1996).
7. W. Götz, *Mater. Res. Soc. Symp. Proc.* **378**, 491 (1995).
8. W. Götz, N. M. Johnson, D. P. Bour, C. Chen, H. Liu, C. Kuo, and W. Imler, *Mater. Res. Soc. Symp. Proc.* **395**, 443 (1996).
9. N. M. Johnson, in *Hydrogen in Semiconductors*, J. L. Pankove and N. M. Johnson, eds. (Academic, San Diego, Calif., 1991), p. 118.

5. MICROELECTRONICS

5.1 ADAPTIVE IMAGING WITH AN ORTHOGONAL-TRANSFER CCD

Recently, we described a new charge-coupled device (CCD) structure capable of transferring charge in four directions and demonstrated its performance with a 64 × 64-pixel prototype imager [1],[2]. The application that motivated this device was adaptive imaging in ground-based astronomy where we believed the orthogonal-transfer (OT) CCD could partially correct for the effects of atmospheric turbulence that degrade image resolution. In particular, the device could remove the lowest-order phase distortion, namely, the so-called tip/tilt distortion, that produces random translation of a celestial image on the focal plane. The prototype device was too small to be useful for such an application, but recently we designed and fabricated a larger-format device. This report describes a 512 × 512-pixel frame-transfer OTCCD as well as some results of recent field tests at the Michigan-Dartmouth-MIT (MDM) 2.4-m telescope on Kitt Peak.

Figure 5-1 depicts the pixel structure and the operating modes for horizontal and vertical charge transfer. The device is built with four gate levels, two of which are triangular in shape. When the level-4 gates are biased low they act as channel stops, and the remaining three gates can be used to clock charge vertically in a conventional three-phase manner. Conversely, charge can be clocked in the horizontal direction by biasing the level-3 gates low and clocking levels 1, 2, and 4. This structure was incorporated into the imaging area of a 512 × 512-pixel frame-transfer device where the frame store had conventional

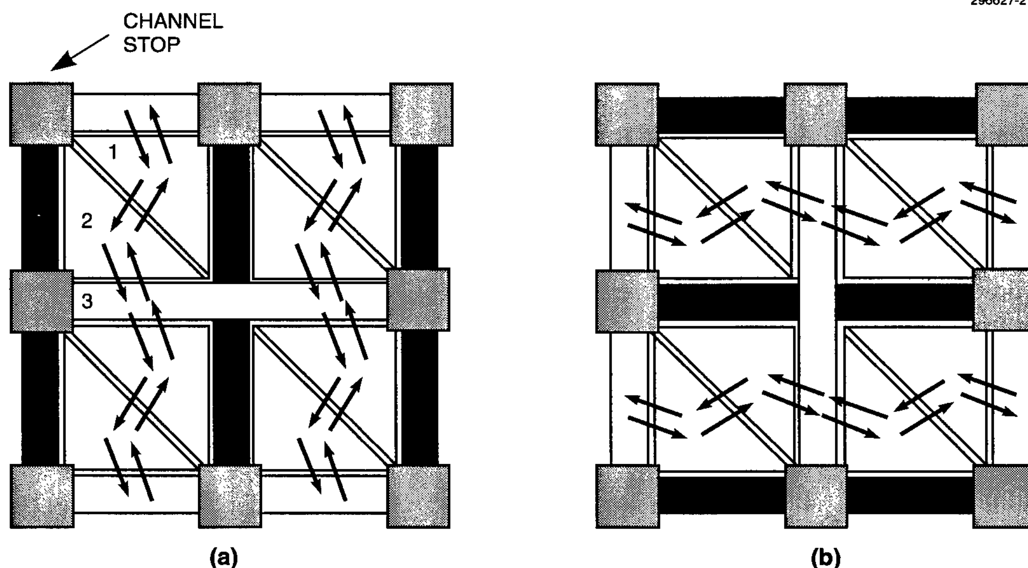

Figure 5-1. Basic cell layout of the orthogonal-transfer charge-coupled device (OTCCD), and modes of clocking for (a) vertical and (b) horizontal charge transfer.

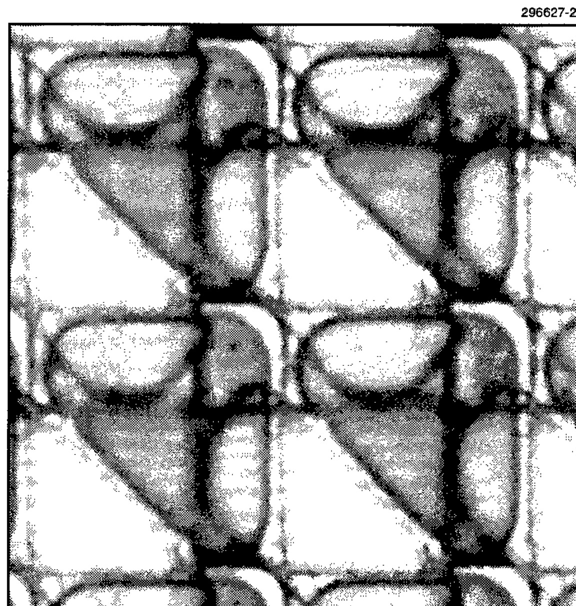

Figure 5-2. Photograph showing four pixels in imaging array of OTCCD. The pixel size is 15 × 15 μm.

three-level, three-phase gates. The pixel size is 15 × 15 μm in both imaging and frame-store regions. Since the CCD fabrication process had only three polysilcon gate levels, we chose for expediency to use the aluminum that forms the clock lines and bonding pads as the fourth gate level. Figure 5-2 shows a photograph of four pixels in the imaging area. The lighter triangular phase-2 gates are aluminum.

Figure 5-3 illustrates the technique used to perform the tip-tilt correction in the field tests. The frame store on this device was not covered by an opaque light shield (unlike conventional frame-transfer devices) so that it could be used as a fast star tracker. A suitably bright star is selected and its motion is tracked by reading out a small subarray around the star at frame rates up to 100 Hz. This motion is then used to shift the imaging clocks to maintain registration between the charge packets and the moving image. This electronic tip/tilt correction offers significant advantages over methods that involve rapidly tilted mirrors in the optical path. Conventional tip/tilt correctors are expensive, involve optical loss, and must be carefully designed to avoid mechanical resonances.

The OTCCD was tested in this mode at the MDM observatory in July 1996. Figure 5-4 shows a 100 × 100-pixel subarray of a portion of the globular cluster M71. In both cases the integration time was 150 s and the device was cooled to approximately –100°C. The image in Figure 5-4(a) was taken in the normal CCD mode with the imaging clocks stationary during the integration time, while Figure 5-4(b) was acquired using the guided OT capability. The frame store in this case was operated at a 7-Hz frame rate, and 1113 charge transfers were used to guide the imaging array. A comparison of the images shows

a significant improvement in resolution and signal-to-noise ratio (SNR). Note in particular how the bright stars near the upper left and right edges are resolved into multiple stars as a result of the improved seeing. The star images in Figure 5-4(a) have a full width at half-maximum (FWHM) of 0.73 arc sec, while in Figure 5-4(b) the OTCCD has reduced this to 0.50 arc sec. The OTCCD has increased the SNR, which is proportional to $1/FWHM^2$, by a factor of 2.1, and this is effectively the equivalent of doubling the primary mirror area. Additional measurements taken under a variety of seeing conditions show that the OTCCD decreases the FWHM by ~ 0.5 arc sec in quadrature with the remaining sources of image broadening [3].

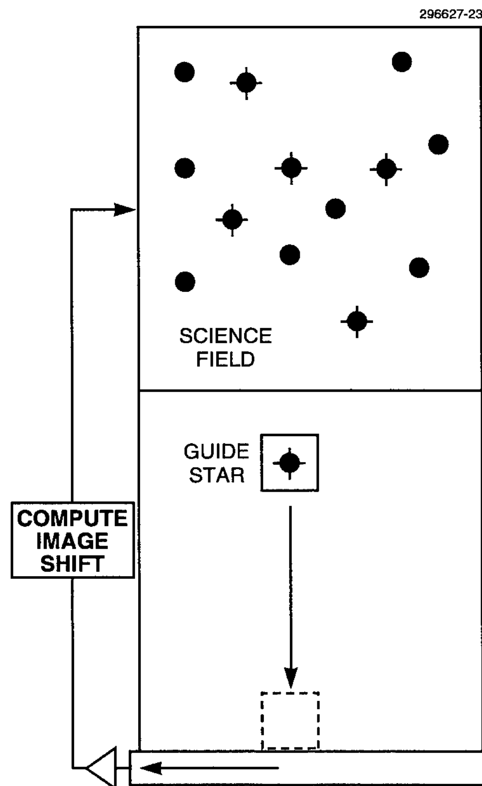

Figure 5-3. Operation of OTCCD as adaptive sensor for tip/tilt correction of astronomical images. The frame store is used as a fast star tracker to follow the image motion, and this information is used in turn to clock the imaging array gates.

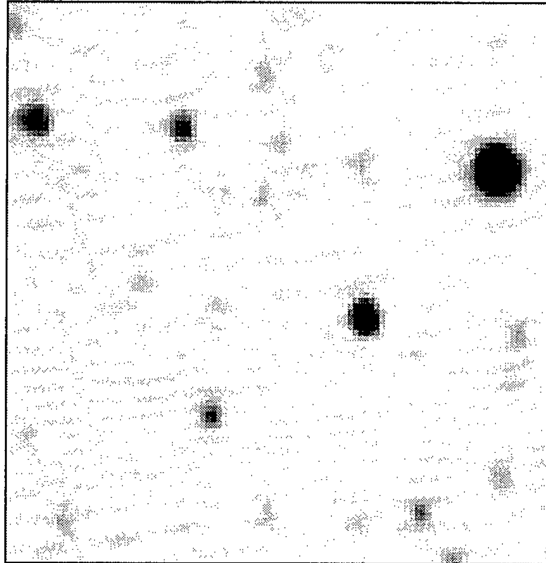

(a)

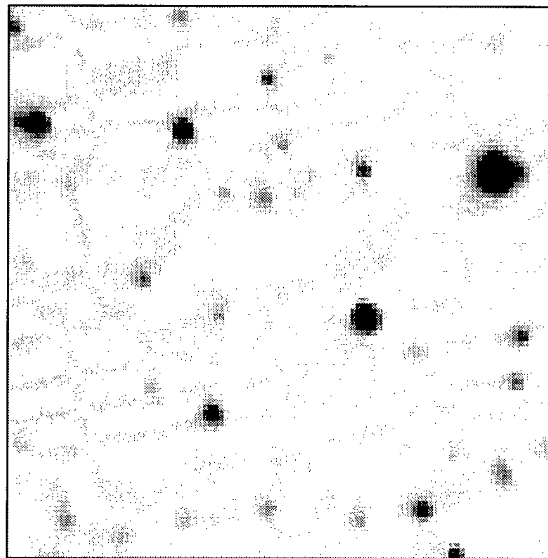

(b)

Figure 5-4. Portion of image of M71 using (a) standard clocking and (b) the adaptive clocking method illustrated in Figure 5-3. The image resolution on the top has a full width at half-maximum of 0.73 arc sec, while on the bottom this has been improved to 0.50 arc sec.

The OTCCD has other potential applications, such as imaging from space platforms. A variety of vibration sources are found on satellites, such as momentum wheels, solar-panel motion, and scanning mirrors; and sensors that have integration times longer than the periods of these vibrations may need elaborate mechanical isolation from the host platform. An OTCCD can compensate for such motion with the potential for significant cost and weight savings.

B. E. Burke
J. L. Tonry*

REFERENCES

1. Solid State Research Report, Lincoln Laboratory, MIT, 1994:1, p. 35.
2. B. E. Burke, R. K. Reich, E. D. Savoye, and J. L. Tonry, *IEEE Trans. Electron Devices*, **41**, 2482 (1994).
3. J. T. Tonry, B. E. Burke, and P. L. Schechter, to be published in *Publ. Astron. Soc. Pacific.*

*Author not at Lincoln Laboratory.

6. ANALOG DEVICE TECHNOLOGY

6.1 SUPERCONDUCTIVE PATCH RESONATOR FOR MICROWAVE HIGH-POWER FILTERS

One of the promising applications of high-T_c superconductor thin films is in the fabrication of narrowband microwave filters with very sharp skirts, which can be used to minimize out-of-band signals created by the nonlinear behavior of high-power amplifiers for transmit applications. An example is that of cellular base stations. Typical peak powers for these applications are near 100 W. In the past we have reported on the design and measurement of high-power filters based on low impedance microstrip line resonators [1]. These filters' performance, however, fell short of the desired power-handling goal. In this report, we describe a novel resonator structure which may provide the desired power handling.

The power handling of microstrip resonators is severely limited by current crowding at the edges of the lines. Because of the small penetration depth of the electromagnetic radiation in superconductors, of the order of 2000 Å for yttrium barium copper oxide, the current density at the edges of a 3-mm-wide line is close to 100 times the average current density in the line. A number of patch-resonator structures have been proposed for conventional planar microwave filters as a way to minimize their loss. These same structures when used with superconductors have the potential to improve the power handling of filters by alleviating the current crowding at the edges.

For microwave filters based on microstrip lines, we use the characteristic impedance of the lines to relate the current in the resonators to the output power in the filters. Therefore, power-handling measurements of resonators can be easily extrapolated to the power handling of filters synthesized using similar resonators. For patch resonator filters, the same concepts cannot be applied. However, it is possible to show [2] that, analogous to the general concept of Q, we can define a Q_{local} for each resonator in the filter as

$$Q_{\text{local}} = \frac{\omega_0 \times \text{Energy stored in the resonator}}{2 \times \text{Average power transmitted}} , \tag{6.1}$$

where ω_0 is the resonance angular frequency. Also, it can be shown that for a particular filter design, Q_{local} is independent of the type of resonator used to implement the filter. If we use this concept for a single resonator, we can show [2] that

$$E_0 \omega_0 = \frac{2 P_{\text{rms out}} \times Q_u}{\gamma_v} , \tag{6.2}$$

with IL = 20log γ_v and where Q_u is the unloaded Q and IL the insertion loss of the resonator in dB's. The quantity $E_0\omega_0$ is usually referred to as the circulating power for the resonator.

From the measurements of the loaded Q of the resonator we can calculate Q_u by

$$Q_u = \frac{Q_{\text{loaded}}}{1-\gamma_v} \quad . \tag{6.3}$$

So by measuring Q_{loaded} and IL as a function of input power, we can calculate both Q_u and the circulating power.

For an n-pole filter

$$\left(P_{\text{rms out}}\right)_{\max} = \frac{2\eta \times \omega_0 \times E_{0_{\max}}}{G_K} \quad , \tag{6.4}$$

where η is the fractional bandwidth and G_K is the largest of the elements for the low-frequency prototype used in the synthesis of the filter.

The criteria for defining $E_{0_{\max}}$ for the resonator is based on the desired performance for the filter. For superconductive filters, the limiting factor is usually the power dissipated in the filter, which must be removed by the cryocooler. Even for an insertion loss of 0.1 dB, very low by conventional standards, 2.3% of the input power is being dissipated by the filter. The insertion loss of a filter at the center frequency can be calculated by

$$\text{IL} = \frac{4.84\sum_{L=1}^{n} G_L}{\eta Q_{\text{unloaded}}} \quad , \tag{6.5}$$

where G_L are elements obtained from the low-frequency prototype for the filter.

Once a maximum IL for a filter is chosen, expression (6.3) allows the minimum acceptable Q_u to be calculated.

We show in Table 6-1 the relative circulating power for circular, elliptical, and 10-W microstrip lines resonating at 2 GHz. We also show the results for what we call the lime resonator, shown in Figure 6-1. These measurements were made using an Nb thin film resonator on $LaAlO_3$. We used Nb because it is easier to make films with very reproducible properties, and we were interested in determining the effect of the shapes of the resonators. Also, for Nb, the onset of nonlinear behavior is very sharp, and $E_{0_{\max}}\,\omega_0$ can be determined easily. We see that the lime had the best power-handling characteristics, followed by the circle.

Circular resonators, because of symmetry, have two orthogonal modes with the same resonant frequency. Any small imperfection on the disc will lead to mode coupling, resulting in two adjacent maxima on the frequency response of the resonator. Strong input-output coupling to the resonator will break the symmetry, resulting in a single resonance, but our experiments show that for the interresonator coupling strength necessary for narrowband filter synthesis, the two peaks will be present and circular resonators cannot be used. The lime resonator does not suffer from the same limitation.

In Figure 6-2 we plot Q_u and the circulating power for the lime resonator shown in Figure 6-1. This resonator was fabricated using sputtered films of YBCO deposited on both sides of an $LaAlO_3$ substrate

TABLE 6-1

Relative Circulating Power for Various Resonators

Resonator	Relative Power
10-Ω Microstrip	1.0
Circular	10.5
Elliptical	6.84
Lime	11.0

296627-25

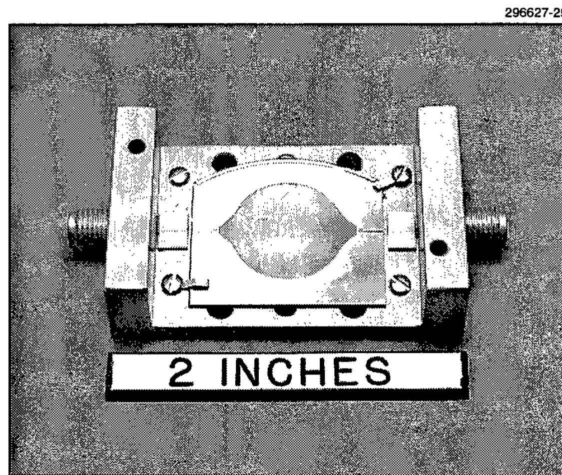

Figure 6-1. Lime resonator made using sputtered YBCO films deposited on both sides of $LaAlO_3$ substrate.

[3]. From the figure, we see that for a lime resonator operating at 40 K and a Q_u of 20 000 a circulating power of 69 dBm is obtained. A nine-pole filter with a bandwidth of 1% and a ripple of 0.1 dB built using a similar resonator would handle 75 W with an insertion loss of 0.35 dB at the middle of the band.

The unloaded Q values shown in Figure 6-2 are smaller than expected. These resonators were built with films of YBCO deposited on both sides of an $LaAlO_3$ substrate. They are tested in an evacuated cryocooler, and thus it is necessary to thermally anchor the resonator and package to the cryocooler. This is accomplished by depositing a thin film of silver on the unpatterned side of the resonator, annealing this film at 400°C, and using a Sn-In eutectic solder to attach the resonator to an expansion-matched Ti package. We suspect that this process is damaging the ground plane. The validity of this hypothesis is strengthened by the measurements made on resonators built on YBCO patterned films, but using Nb

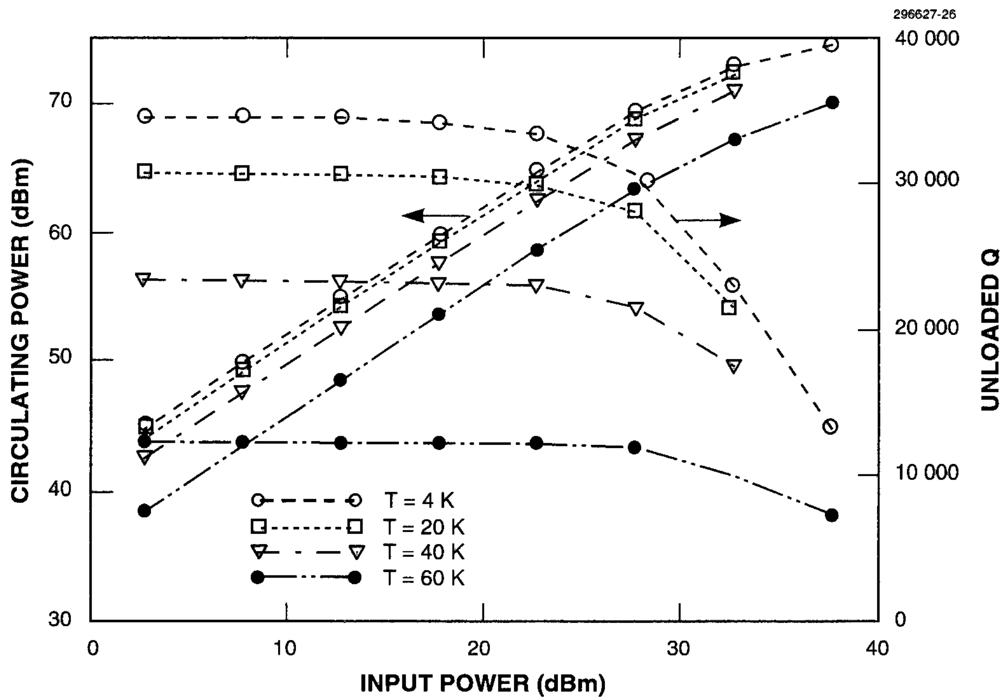

Figure 6-2. Circulating power (left axis) and unloaded Q (right axis) as a function of input power for resonator shown in Figure 6-1.

expansion-matched Ti ground planes. Their Q_u values were larger than 130 000 at 4K. New methods for attaching the substrate to the package are being examined.

A. C. Anderson
R. L. Slattery
R. R. Boisvert

REFERENCES

1. Solid State Research Report, Lincoln Laboratory, MIT, 1996:2, p. 29.
2. G. L. Matthaei, L. Young, and E. M. T. Jones, *Microwave Filters, Impedance-Matching Networks, and Coupling Structures* (McGraw-Hill, New York, 1964).
3. Solid State Research Report, Lincoln Laboratory, MIT, 1993:2, p. 32.

7. ADVANCED SILICON TECHNOLOGY

7.1 FULLY PLANAR MULTILEVEL METAL INTERCONNECT

The primary drivers for employing a multilevel interconnect scheme in advanced CMOS processing include increasing the functional density of circuits and reducing RC delay [1]. Functional density refers to the number of transistors that can be wired together to perform circuit operations. The sharing of interconnect between levels allows this quantity to increase. RC delay is proportional to the square of the line length. By using multiple levels of interconnect, wiring together of circuit elements can follow more direct paths and thus overall line length decreases.

Because of increasingly scaled circuits and the growing number of metallization levels, advanced back end of the line (BEOL) fabrication techniques are needed. These techniques include: dielectric gap fill between conductors, planarization of levels to accommodate reductions in depth of focus and to reduce metal stringers, vertical walled contacts and vias to increase packing density, and damascene aluminum plugs at contact and via levels followed by aluminum-based interconnect deposition and patterning. We have developed a BEOL process in the Microelectronics Laboratory that utilizes these features. The process is used to support the advanced CMOS projects in the Laboratory and was successfully implemented in the first silicon-on-insulator multi-project run.

As devices are scaled, metal lines become more narrow and closely packed, but do not necessarily become thinner because of the need for low-resistance conductors. This leads to large aspect ratios (ratios of conductor thickness to space width) which are difficult to fill with dielectric. The intermetal dielectric is plasma deposited tetraethylorthosilicate (TEOS) based silicon dioxide. Because of the low deposition temperature (300°C), the surface mobility of the depositing film is low and films tend to be thicker along horizontal surfaces than on the vertical surface of the underlying wafer topography [2]. Owing to geometrical shadowing during dielectric deposition, voids can form between metal lines; voids can become a reliability problem if exposed during subsequent processing. One method of solving this problem involves alternating cycles of deposition with argon sputter etch back. This deposition/etch process removes material at the line corners and prevents the film from closing off and forming voids. Our deposition/etch process utilizes four cycles followed by a thick capping layer. The process ensures good gap fill to aspect ratios of 1.35, while a standard deposition begins voiding off at an aspect ratio of 0.95, as shown in Figure 7-1.

As devices are scaled, the lithography depth of focus decreases. In addition, growing topography makes it difficult to etch stringer-free conductors. Stringers can cause lateral shorts between conductor lines. Because of these issues, it becomes increasingly important to planarize interlevel dielectrics at each level [3]. Chemical-mechanical planarization (CMP) is one method that allows for global planarization (millimeter scale), as shown in Figure 7-2. Topography reduction is effected by chemical and mechanical action through the combined use of a silica abrasive suspended in an alkaline solution, and polyurethane polishing pads. In the process developed, both the poly-metal and intermetal dielectrics are planarized. Because of pattern dependencies, CMP causes intradie interlevel dielectric thickness variations. Careful measurement of this variation is required to ensure complete contact and via etches.

296627-27

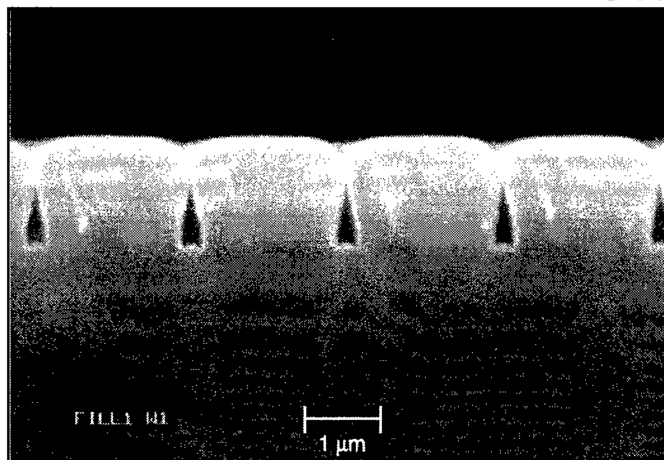

(a)

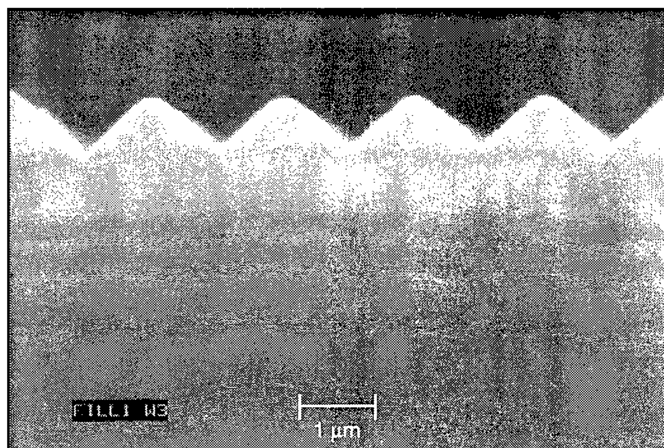

(b)

Figure 7-1. Scanning electron micrograph cross section of dielectric gap fill: (a) standard deposition, aspect ratio ~ 0.95; (b) multiple deposition/etch back process, aspect ratio ~ 1.35.

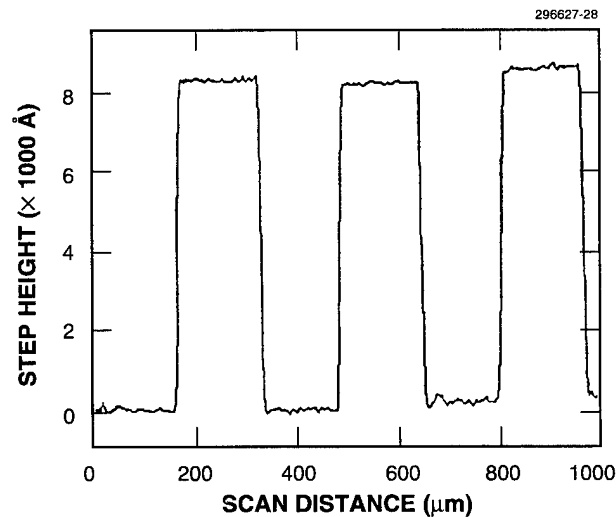

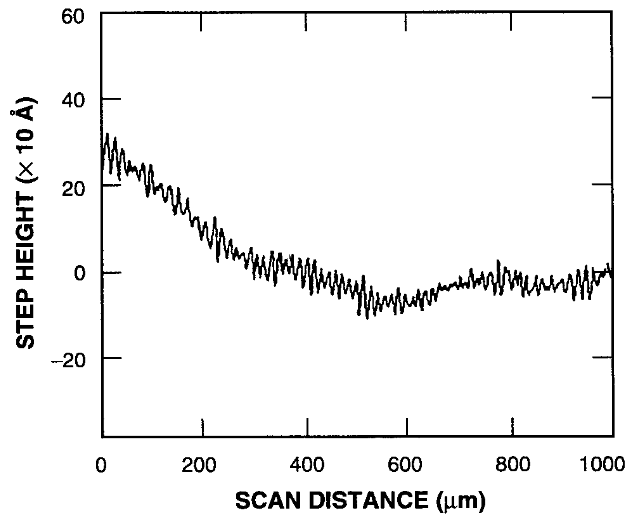

Figure 7-2. Chemical-mechanical planarization (CMP) step height reduction. Measurements shown are (a) before and (b) after CMP.

Vertical-walled contact and via etches are employed to increase packing density. They also have the advantage of a larger overetch latitude than sloped-walled versions, owing to the slower consumption of the photoresist mask during the etch. Long overetches are necessary because of the cross-wafer and intradie interlevel dielectric variations induced by CMP. Because the contacts and vias are vertical, a metal plug process is required to ensure good electrical connection to the underlying level. Also, post-etch polymer residues must be completely removed so that they don't affect the plug process.

After the vias and contacts are etched, aluminum plugs are fabricated by high-temperature sputtering (500°C) which causes the metal to flow into the high-aspect-ratio contact and via holes. Hot aluminum plug fill is preceded by deposition of a diffusion barrier (100 nm of collimated, biased TiN, at 450°C) and a wetting layer (30 nm of collimated Ti, at 450°C). After deposition of the plug, CMP is used to remove metal in the field regions. The interlevel dielectric serves as a stopping layer with an aluminum-to-oxide selectivity of 30 to 1. Aluminum damascene plug formation is followed by the deposition and patterning of the 150°C aluminum-based interconnect stack, which consists of Ti:Al(1%Si):Ti:TiN (40 nm: 500 nm: 40 nm: 50 nm). The lower-temperature interconnect metal ensures a smooth surface, which is important for proper interconnect lithography. Because of the high selectivity of the aluminum damascene plug process and the minimal plug dimensions, there is very little plug recess. The interconnect surface remains planar, which allows contacts and vias to be stacked and packing density to increase, as shown in Figure 7-3.

296627-29

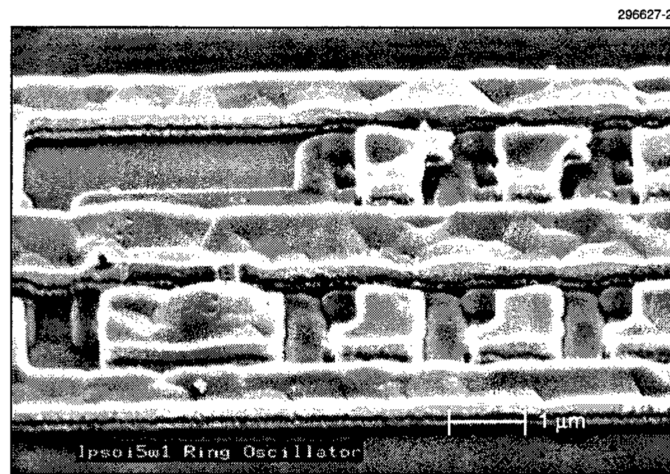

(a)

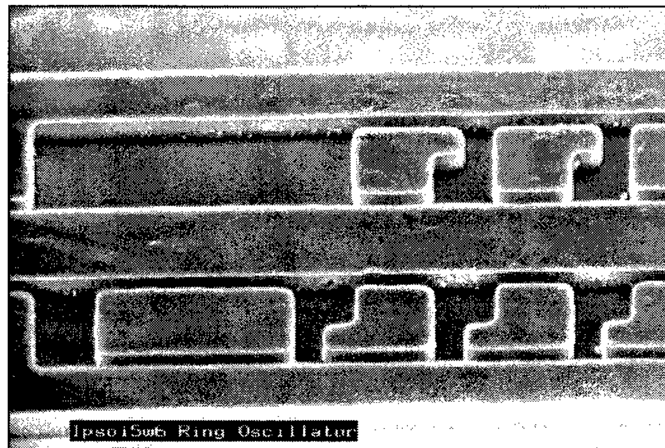

(b)

Figure 7-3. Comparison of (a) nonplanar and (b) planar interconnect in silicon-on-insulator ring oscillator.

The test vehicle for this process was a two-level metal data-thinning circuit containing ~ 5000 transistors. Contact and via sizes were 0.5 and 0.75 μm, respectively. Metal-1 linewidth is 0.75 μm; metal-2 is 1.0 μm. Targeted thicknesses of dielectrics were 0.55 μm over silicon island (0.45 μm over poly) and 0.75 μm between metal 1 and metal 2. Every level in the fabrication process used 248-nm lithography. The application calls for 800-MHz circuit operation at 2 V. In fact, the successfully fabricated circuit operated at > 1 GHz at 2 V. While the circuit application described contains only two levels of metal, it should be noted that repeated application of this process module can be used to add further levels. Three levels of metal have been successfully fabricated on test wafers, and this process is currently being incorporated in an enhanced version (18 000 transistors) of the data-thinning circuit.

J. M. Knecht

REFERENCES

1. S. Wolf, *Silicon Processing for the VLSI Era. 2. Process Integration* (Lattice Press, Sunset Beach, Calif., 1990).

2. E. McInerney and S. Avanzino, *IEEE Trans. Electron. Devices* **ED-34**, 615 (1987).

3. S. Sivaram, H. Bath, R. Leggett, A. Maury, K. Monnig, and R. Tolles, *Solid State Technol.* **35**, 87 (1992).

REPORT DOCUMENTATION PAGE

Form Approved
OMB No. 0704-0188

Public reporting burden for this collection of information is estimated to average 1 hour per response, including the time for reviewing instructions, searching existing data sources, gathering and maintaining the data needed, and completing and reviewing the collection of information. Send comments regarding this burden estimate or any other aspect of this collection of information, including suggestions for reducing this burden, to Washington Headquarters Services, Directorate for Information Operations and Reports, 1215 Jefferson Davis Highway, Suite 1204, Arlington, VA 22202-4302, and to the Office of Management and Budget, Paperwork Reduction Project (0704-0188), Washington, DC 20503.

1. AGENCY USE ONLY (*Leave blank*)

2. REPORT DATE
15 February 1997

3. REPORT TYPE AND DATES COVERED
Quarterly Technical Report, 1 November 1996–31 January 1997

4. TITLE AND SUBTITLE
Solid State Research

5. FUNDING NUMBERS
C — F19628-95-C-0002
PE — 63250F
PR — 221

6. AUTHOR(S)
David C. Shaver

7. PERFORMING ORGANIZATION NAME(S) AND ADDRESS(ES)
Lincoln Laboratory, MIT
244 Wood Street
Lexington, MA 02173-9108

8. PERFORMING ORGANIZATION REPORT NUMBER
1997:1

9. SPONSORING/MONITORING AGENCY NAME(S) AND ADDRESS(ES)
HQ Air Force Materiel Command
AFMC/STSC
Wright-Patterson AFB, OH 45433-5001

10. SPONSORING/MONITORING AGENCY REPORT NUMBER
ESC-TR-96-125

11. SUPPLEMENTARY NOTES
None

12a. DISTRIBUTION/AVAILABILITY STATEMENT
Approved for public release; distribution is unlimited.

12b. DISTRIBUTION CODE

13. ABSTRACT (*Maximum 200 words*)

This report covers in detail the research work of the Solid State Division at Lincoln Laboratory for the period 1 November 1996–31 January 1997. The topics covered are Electrooptical Devices, Quantum Electronics, Materials Research, Submicrometer Technology, High Speed Electronics, Microelectronics, and Analog Device Technology. Funding is provided primarily by the Air Force, with additional support provided by the Army, DARPA, Navy, BMDO, NASA, and NIST.

14. SUBJECT TERMS
quantum electronics, electrooptical devices, materials research, submicrometer technology, high-speed electronics, microelectronics, analog device technology, advanced silicon technology, optical frequency converters, analog optical links, lasers, nanochannel fabrication, charged-coupled devices, microwave filters, CMOS processing

15. NUMBER OF PAGES
74

16. PRICE CODE

17. SECURITY CLASSIFICATION OF REPORT	18. SECURITY CLASSIFICATION OF THIS PAGE	19. SECURITY CLASSIFICATION OF ABSTRACT	20. LIMITATION OF ABSTRACT
Unclassified	Same as Report	Same as Report	Same as Report

NSN 7540-01-280-5500

Standard Form 298 (Rev. 2-89)
Prescribed by AMSI Std. 239-18
298-102